



Liquefaction induced permanent ground deformations and energy dissipation analysis based on smoothed particle hydrodynamics method (SPH): validation by large-scale model tests

Mohammad Sadegh Maghsoudi¹ · Reza Jamshidi Chenari² · Farhang Farrokhi¹

Received: 17 April 2022 / Accepted: 25 July 2022 / Published online: 5 September 2022
© The Author(s), under exclusive licence to Springer-Verlag GmbH Germany, part of Springer Nature 2022

Abstract

To accurately simulate the permanent displacements caused by liquefaction in saturated sandy soils, a mesh-free method named smoothed particle hydrodynamics (SPH) with a suitable soil behavior model and considering the interaction between soil and water phases has been developed in this study. The considered soil–water coupled phase plays the most critical role in more accurate modeling of soil failure during liquefaction and post-liquefaction processes. The results of the developed SPH code have been validated in the present study by performing some large-scale model tests in the laboratory using a shaker and a shaking table. The comparison between the SPH simulated displacement and the results of shaking table tests showed a good agreement, which proved that the proposed SPH framework could be a suitable tool for simulating and estimating the liquefaction-induced displacements. Moreover, the shear stress–strain response and subsequently the energy dissipated in soil were investigated in the shaking table test setting and a close correlation was observed between the excess pore water pressure and energy dissipation during liquefaction.

Keywords Smoothed particle hydrodynamics · Liquefaction · Energy dissipation · Permanent displacements · Shaking table · Quick tank

1 Introduction

Liquefaction-induced permanent ground deformation is a typical consequence of reduced shear strength of loose saturated sandy soils due to excess pore water pressure during earthquakes. This type of failure, which is usually perceived as an aftermath of strong earthquakes, often involves large deformations, especially in problems related to instabilities

associated with the liquefaction in slopes and embankments. Due to the destructive nature and extensive damages to structures and infrastructures, estimation of these deformations has always been of concern, and a plethora of research have recently been presented in this field. Among these studies, the efforts based on computational approaches remain an active and progressive area of debate in geotechnical engineering due to their high versatility and remarkable accuracy.

There are several studies in the literature in which mesh-based numerical methods have been used to model the large displacements due to liquefaction. The most significant of these studies include those using the Finite Element Method [1–3], Finite Difference Method [4–6], and Finite Volume Method [7]. The accuracy of modeling in mesh or grid-based methods is often dependent on the geometry of the grid. When this geometry becomes too distorted, the accuracy of the numerical solution decreases sharply, and even the computational process may fail. In the same way, for extensive deformation and the flowing of geomaterials, it is sometimes experienced that FEM

This article is part of a topical collection: Energy transport and dissipation in granular systems.

✉ Reza Jamshidi Chenari
Jamshidi_reza@guilan.ac.ir

Mohammad Sadegh Maghsoudi
maghsoudi@znu.ac.ir

Farhang Farrokhi
Farhang.Farrokhi@znu.ac.ir

¹ Department of Civil and Environmental Engineering, Faculty of Engineering, University of Zanjan, Zanjan, Iran

² Department of Civil Engineering, Faculty of Engineering, University of Guilan, P.O. 3756, Rasht, Guilan, Iran

simulations fail due to the mesh distortion and negative values of the Jacobian determinants of the nodes [8].

An alternative to grid-based numerical methods is mesh-free methods. As the name implies, in such practices, the equations of motion are solved for a set of particles without any dependence on a grid or mesh. The obvious advantage of these approaches is that a Lagrangian frame is selected. It is possible to track the history-dependent material without the mesh entanglement and loss of computational accuracy due to highly deformed grids. This feature has recently been demonstrated by some researchers in simulating geotechnical problems, especially those related to large deformations [8–11].

The Discrete Element Method (DEM), as the oldest particle-based approach used in geotechnical problems, has been the subject of research by several researchers in the field of geotechnical failure modeling, including soil liquefaction deformations [12–15]. In DEM, particles are moved according to the contact force modeled by a spring and dashpot system [16], and there is no need to implement a continuum-based constitutive model. Despite the appropriate performance of this method for large deformation analysis of geomaterials, some typical and practical problems that consist of too many particles demand enormous computational efforts that detracts from its real merits in practice.

Due to the deficiencies attributed to the methods pointed out above, another meshless method called, Smoothed Particle Hydrodynamics (SPH), is considered. The SPH method is a particle method based on a mesh-free Lagrangian scheme that describes the domain of interests as a continuum. The advantage of the SPH Lagrangian method is that the mesh is deformed with the material, and therefore, it is easy to track the moving boundary and interfaces. This method has recently been of interest to many researchers to simulate various geotechnical engineering problems [17–21]. During these researches, good results were obtained using different constitutive models and the theories based on multi-phase environment modeling according to each specific problem.

Nguyen et al. [9] investigated the mobility of granular flow, as a large-scale deformation problem, through granular column collapse experimental tests using the Smooth Particle Hydrodynamics (SPH) method. In their study, the effect of material properties of granular media have been investigated on the deposit morphology, energy dissipation, and run-out distance of granular flow, and there was a good agreement between the numerical and experimental results. Salehizadeh and Shafiei [11] numerically studied the same granular collapse problem using a local rheology model in a proposed 2-D SPH algorithm validated by analytical solution and experimental tests. The results of the study showed that the applied method has a good ability to

simulate granular flow, especially in front of the flow, which has a large deformation and high velocity.

Despite the many advantages and exceptional results obtained from using the SPH method in the above studies, some problems when simulating geomaterials have been reported. For example, in some cases, SPH suffers from instability and inaccuracy problems, such as the oscillation of the pressure field and the deficiency of boundary particles [22].

This research aims to use the SPH method to simulate the liquefaction-induced permanent ground deformations, including vertical settlements and large lateral displacements. The elastic-perfectly plastic material behavior using the Drucker-Prager failure criterion has been deployed to simulate the soil continuum in the developed code; soil–water interaction scheme based on the effective stress concept was selected as a suitable approach for accurate simulation of liquefied soil deformations. The validation of the current SPH code is then carried out using model tests performed on a shaker and a shaking table for different liquefaction-induced ground deformations. The effect of soil relative density on the vertical settlements of a uniform soil layer has been investigated and the role of excess pore water pressure development on the settlement values are discussed. Also in the shaking table test setting where the soil profile undergoes large strains, the stress–strain behavior of soil is investigated and the possible relationship between the excess pore water pressure and the energy dissipated due to the dynamic loading is evaluated.

2 Basic concepts and formulation of SPH method

The SPH method is based on the principle that the domain of interest is discretized by an assembly of particles representing the field quantities, such as mass, density, and velocity. In this method, the quantities are obtained at individual discrete points. The general behavior of the domain is determined using integration over the domain, which is done by summation over the neighboring particles. To achieve this process, a kernel estimation function is usually used. Kernel function refers to a weight function that defines how much the field quantities contribute to each other. Considering a field function f defined in a domain Ω , the kernel function is defined as:

$$f(x) = \int_{\Omega} f(x') W(\mathbf{x} - \mathbf{x}', h) dx' \quad (1)$$

where the kernel function, denoted as $W(x - x', h)$ derived from the Dirac delta function, $\delta(\mathbf{x} - \mathbf{x}')$, and is a

non-negative function that is centered at point \mathbf{x} and uniformly decreases with the distance $|\mathbf{x} - \mathbf{x}'|$, and h represents the smoothing length.

To use Eq. (1) in the numerical simulation process, the computational domain should be discretized into a finite number of integration points (also called particles), and it can be expressed in the form of summation over all particles in the support domain as follows:

$$f(x_i) = \sum_j f(x_j) \frac{m_j}{\rho_j} W(r_{ij}, h) \tag{2}$$

$$\frac{\partial f(x_i)}{\partial t} = \sum_j f(x_j) \frac{m_j}{\rho_j} \frac{x_i - x_j}{r_{ij}} \frac{\partial W(r_{ij}, h)}{\partial r_{ij}} \tag{3}$$

where the subscript i denotes the desired particle, and the subscript j represents the particles in the neighborhood of the particle i . In Eqs. (2) and (3), r_{ij} is the distance between the particles i and j , and field variables are m, ρ , and f , which represent the mass, density, and body force, respectively. The mathematical formulation and other details of the SPH method can be found in the technical texts [22].

The kernel function W has a support domain of radius κh , a multiple of the smoothing length, h , and determines the number of neighboring particles involved in the approximation (see Fig. 1). The value of the constant κ is determined depending on the smoothing kernel type. The above characteristics of the SPH method and, in particular, the local dependence on the support domain updated at every step with the addition of the Lagrangian formulation allows SPH to model problems with high deformation such as landslide flows and liquefaction induced extensive ground failures.

The choice of kernel type directly affects the accuracy, efficiency, and stability of the SPH simulation process, and

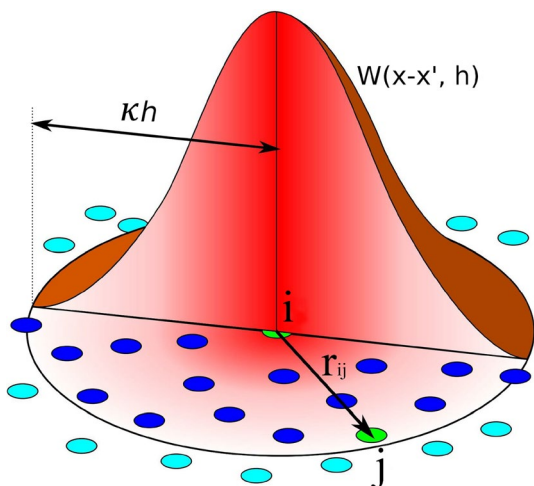


Fig. 1 Kernel function W and its support domain

various researches have been done in this field [23–25]. The most common and well-known kernel is the 'cubic spline' function proposed by Monaghan [26] and is expressed by the following equation:

$$W_{ij}(r) = \alpha \begin{cases} 1 - \frac{3}{2}q^2 + \frac{3}{4}q^3; & 0 \leq q \leq 1 \\ \frac{(2-q^3)}{4}; & 1 < q \leq 2 \\ 0; & \text{elsewhere} \end{cases} \tag{4}$$

where $q = r/h$, r is the relative distance between particles i and j as $r = |r_i - r_j|$, and α is a coefficient equal to $(10/7)\pi h^2$ for two-dimensional space [27].

Typically, the motion of the particles is simulated in the SPH method using the governing equations of continuity and momentum, which describe the conservation of mass and momentum, respectively. These two basic equations are defined as follows:

$$\text{Continuity equation : } \frac{D\rho}{Dt} = -\rho \frac{\partial v^\alpha}{\partial x^\alpha} \tag{5}$$

$$\text{Momentum equation : } \frac{Dv}{Dt} = \frac{1}{\rho} \frac{\partial \sigma^{\alpha\beta}}{\partial x^\beta} + g^\alpha \tag{6}$$

In Eqs. (5) and (6), ρ is the density of the soil particles, v is the velocity, $\sigma^{\alpha\beta}$ is the stress tensor calculated from the constitutive model, and g is the gravitational acceleration. Also, the superscripts α and β , are used to denote the coordinate direction.

By using Eq. (3), the discrete representation of the continuity equation for water and soil particles, to use in the SPH framework, is obtained as Eq. (7).

$$\frac{d\rho_i}{dt} = \rho_i \sum_j \frac{m_j}{\rho_j} v_{ij} \frac{\partial W_{ij}}{\partial x_a^\alpha} \tag{7}$$

Also, the momentum equation is derived separately for water and soil particles as follows.

$$\begin{aligned} \text{For water particles: } \frac{dv_i^\alpha}{dt} = & - \sum_j m_j \left(\frac{p_i}{\rho_i^2} + \frac{p_j}{\rho_j^2} \right) \frac{\partial W_{ij}}{\partial x_i^\alpha} \\ & + \sum_j m_j v_{ij}^\alpha \left(\frac{\mu_i}{\rho_i^2} + \frac{\mu_j}{\rho_j^2} \right) \frac{\partial W_{ij}}{\partial x_i^\alpha} + f_i^\alpha \end{aligned} \tag{8}$$

$$\text{For soil particles : } \frac{dv_i^\alpha}{dt} = \sum_j m_j \left(\frac{\sigma_i^{\alpha\beta}}{\rho_i^2} + \frac{\sigma_j^{\alpha\beta}}{\rho_j^2} \right) \frac{\partial W_{ij}}{\partial x_i^\beta} + f_i^\alpha \tag{9}$$

where $v_{ij}^\alpha = v_i^\alpha - v_j^\alpha$, f_i^α denotes body force, μ is the dynamic viscosity of water, and p is the water pressure obtained by the equation of state (EOS) as follows [27]:

$$p = \frac{\rho_0}{7} c_s^2 \left(\left(\frac{\rho}{\rho_0} \right)^7 - 1 \right) \tag{10}$$

In Eq. (10), c_s is the speed of sound through water, and ρ and ρ_0 are the current and initial water densities, respectively. It is also worth noting that $\sigma^{\alpha\beta}$ in Eq. (9) is the total stress tensor, which consists of an effective stress tensor ($\sigma'^{\alpha\beta}$) and the pore water pressure (p_w) as follows [18]:

$$\sigma^{\alpha\beta} = \sigma'^{\alpha\beta} - p_w I \tag{11}$$

It is assumed that the pore water pressure is negative at compression, and I is the identity matrix.

The effective stress tensor, $\sigma'^{\alpha\beta}$ in Eq. (11) requires an appropriate soil constitutive equation. Any well-known constitutive model can be implemented in the SPH method to calculate stress values caused by particle movements determined from the governing differential equations. Although visco-plasticity constitutive models are highly suitable for simulating granular materials' flow behavior [28–30], the present study has used an elastic-perfectly plastic model as the constitutive model. This soil model will be utilized in the SPH framework by a combination of the hypo-elastic model [31] and the Drucker–Prager's yield criterion [32] as follows:

$$Y(I_1; J_2) = \sqrt{J_2} + \alpha_\phi I_1 - k_c = 0 \tag{12}$$

where I_1 and J_2 are the first invariant of the stress tensor and the second invariant of the deviatoric stress tensors, and α_ϕ and k_c are the Drucker–Prager's constants, which can be obtained in plane-strain conditions as:

$$\alpha_\phi = \frac{\tan\phi}{\sqrt{9 + 12\tan^2\phi}} \text{ and } k_c = \frac{3c}{\sqrt{9 + 12\tan^2\phi}} \tag{13}$$

where c and ϕ are the Coulomb material constants representing the cohesion and internal friction of the soil, respectively.

In deriving the stress–strain relationships of this constitutive model, it is assumed that the total strain rate consists of two elastic and plastic components:

$$\dot{\epsilon}^{\alpha\beta} = \dot{\epsilon}_e^{\alpha\beta} + \dot{\epsilon}_p^{\alpha\beta} \tag{14}$$

where $\dot{\epsilon}_e^{\alpha\beta}$ and $\dot{\epsilon}_p^{\alpha\beta}$ are the elastic and plastic strain rate tensors, respectively. The elastic strain rate is calculated by generalized Hooke's law given that the Jaumann rate must be utilized to take the rotational motion of a rigid body [33]:

$$\dot{\epsilon}_e^{\alpha\beta} = \frac{\dot{\sigma}}{D} \Rightarrow \dot{\sigma}^{\alpha\beta} - \sigma^{\alpha\gamma} \dot{\omega}^{\beta\gamma} - \sigma^{\gamma\beta} \dot{\omega}^{\alpha\gamma} = 2G\dot{\epsilon}^{\alpha\beta} + K\dot{\epsilon}^{\gamma\gamma} \delta^{\alpha\beta} \tag{15}$$

D is the elastic stiffness matrix, G is the shear modulus, and K is the bulk modulus. Furthermore, $\dot{\epsilon}^{\alpha\beta}$ and $\dot{\epsilon}^{\gamma\gamma}$ are the

deviatoric and volumetric strain rates, respectively, and $\dot{\epsilon}^{\alpha\beta}$ and $\dot{\omega}^{\alpha\beta}$ denote the total strain rate and spin rate tensors, which are defined in the SPH formulation as follows:

$$\dot{\epsilon}_i^{\alpha\beta} = \frac{1}{2} \sum_j \frac{m_j}{\rho_j} \left\{ (v_j^\alpha - v_i^\alpha) \frac{W_{ij}}{\partial x_i^\beta} + (v_j^\beta - v_i^\beta) \frac{W_{ij}}{\partial x_i^\alpha} \right\} \tag{16}$$

$$\dot{\omega}_i^{\alpha\beta} = \frac{1}{2} \sum_j \frac{m_j}{\rho_j} \left\{ (v_j^\alpha - v_i^\alpha) \frac{W_{ij}}{\partial x_i^\beta} - (v_j^\beta - v_i^\beta) \frac{W_{ij}}{\partial x_i^\alpha} \right\} \tag{17}$$

The plastic strain rate tensor can also be calculated by the plastic flow rule, which is given by the following equation:

$$\dot{\epsilon}_p^{\alpha\beta} = \dot{\lambda} \frac{\partial g_p}{\partial \sigma^{\alpha\beta}} \tag{18}$$

In Eq. (18), g_p and $\dot{\lambda}$ are the plastic potential function and the rate of change of plastic multiplier, respectively, and can be calculated as:

$$g_p = \sqrt{J_2} + 3I_1 \sin\psi \tag{19}$$

$$\dot{\lambda} = \frac{3\alpha_\phi K \dot{\epsilon}_i^{\gamma\gamma} + \left(\frac{G}{\sqrt{J_2}} \right) s_i^{\alpha\beta} \dot{\epsilon}_i^{\alpha\beta}}{27\alpha_\phi K \sin\psi + G} \tag{20}$$

where ψ is the dilatancy angle of the soil.

By combining Eqs. (14) to (20) and then simplification, the final form of the constitutive model will become as:

$$\frac{\partial \sigma_i^{\alpha\beta}}{\partial t} = \sigma_i^{\alpha\gamma} \dot{\omega}_i^{\beta\gamma} + \sigma_i^{\gamma\beta} \dot{\omega}_i^{\alpha\gamma} + 2G\dot{\epsilon}_i^{\alpha\beta} + K\dot{\epsilon}_i^{\gamma\gamma} \delta^{\alpha\beta} - \dot{\lambda}_i \left[9K \sin\psi \delta^{\alpha\beta} + \left(\frac{G}{\sqrt{J_2}} \right) s_i^{\alpha\beta} \right] \tag{21}$$

Typically, two common concerns in most SPH modeling problems are stress fluctuations and tensile instability. These two shortcomings are usually remedied by adding stabilization terms to the momentum equation (Eq. 9) as artificial stress and artificial viscosity. Subsequently, by combining Eqs. (9) and (11) and adding artificial stress and viscosity terms, the final momentum equation for a two-phase system of the soil–water mixture in the form of SPH will be as follows [18]:

$$\frac{dv_i^\alpha}{dt} = \sum_j m_j \left(\frac{\sigma_j^{\alpha\beta}}{\rho_j^2} + \frac{\sigma_j^{\alpha\beta}}{\rho_j^2} + R_i^{\alpha\beta} f_{ij}^n + \Pi_{ij} \delta^{\alpha\beta} \right) \frac{\partial W_{ij}}{\partial x_i^\beta} - \sum_j \frac{m_j}{\rho_i \rho_j} (p_{wj} - p_{wi}) \frac{\partial W_{ij}}{\partial x_i^\alpha} + f_i^\alpha \tag{22}$$

where $R_i^{\alpha\beta} f_{ij}^n$ is the repulsive force term [34] related to the kernel type. Also, the exponent n varies based on the smoothing kernel and is obtained by analysis of dispersion equations. Although it was shown by Gray et al. [35] that $n=4$ would be an optimal choice for elastic solids, Bui et al. [31], after conducting several tests, found that a value of 2.55 was appropriate for elastoplastic materials. Based on this, n in this study was considered to bear a constant value of 2.55. The component $R_i^{\alpha\beta}$ of artificial stress can be calculated as Gray et al. [35]:

$$R_i^{\alpha\beta} = \begin{cases} -\varepsilon \frac{\sigma_i^{\alpha\beta}}{\rho_j^2}, & \alpha = \beta \\ 0, & \alpha \neq \beta \end{cases} \tag{23}$$

where ε is a constant that varies between 0 and 1 and is suggested to be $\varepsilon = 0.3$ in most of the cases [35].

The most common developed equation for calculating artificial viscosity has been proposed by [36]:

$$\Pi_{ij} = \begin{cases} \frac{-\alpha c_{ij} \mu_{ij} + \beta \mu_{ij}^2}{\rho_{ij}}, & v_{ij} x_{ij} < 0 \\ 0, & v_{ij} x_{ij} \geq 0 \end{cases} \tag{24}$$

In this equation, α and β are constants varying between 0 and 1. Monaghan suggests choosing these values close to 1 for best results [34], and c is the sound speed. Other parameters in Eq. (24) are also defined as follows:

$$c_{ij} = \frac{c_i + c_j}{2}, \rho_{ij} = \frac{\rho_i + \rho_j}{2}, h_{ij} = \frac{h_i + h_j}{2}, \tag{25}$$

$$x_{ij} = x_i - x_j, v_{ij} = v_i - v_j \tag{26}$$

$$\mu_{ij} = \frac{h_{ij} v_{ij} \cdot x_{ij}}{r_{ij}^2 + 0.01 h^2} \tag{27}$$

In the above equations, μ is the kinetic viscosity, ρ is the density, h is the smoothing length as also defined earlier, and v and x are the velocity and particle position vectors, respectively.

The soil–water interaction in this study is based on the approach proposed by Bui et al. [32] and improved by Bui and Fukagawa [18], which uses the effective stress concept and pore water pressure. According to this method, soil and water particles co-exist in any location in a two-phase saturated soil mixture, and the motion of particles in each phase is obtained individually using its own SPH momentum equations, Eqs. (8) and (9). The two phases are then superimposed, and the interaction between these phases will be taken into account through the pore water pressure, which is included in the final soil–water mixture momentum equation Eq. (22). As a result, the contribution of pore water pressure

in Eq. (22) makes it possible to simulate its effect on soil particles, and the interaction between the soil and water phases is considered by the SPH simulation accordingly.

The relationship between the deformation and pore water pressure changes is essential when analyzing the saturated soils in geotechnical problems with large deformations. For this reason, porosity and, consequently, permeability in this study is considered as a function of deformation to investigate the effect of changes in pore water pressure on the behavior of saturated soil during liquefaction-induced large displacements. For this purpose, the method proposed by [37] was used. In this method, formulations are based on Biot's two-phase mixture theory along with the updated Lagrangian method as follows.

Therefore, the total stress of saturated soil (σ) can be considered as the sum of the soil skeleton stress (σ_s) and pore water stress (σ_w) as follows:

$$\sigma = \sigma_s + \sigma_w \tag{28}$$

By definition:

$$\sigma_s = \sigma_s' - (1 - n)p_w I \tag{29}$$

$$\sigma_w = -np_w I \tag{30}$$

where n is the soil porosity. The relationship between the water phase stress and velocity can be expressed by the following equation [38]:

$$\dot{\sigma}_w = K_w tr \left(\frac{\partial v_w}{\partial x} \right) I \tag{31}$$

where K_w is the bulk modulus of the fluid and v_w is the velocity of the water particles. It should be noted that in the Lagrangian description, x is the after-deformation position of a soil particle in a time step. A more detailed description of the motion configuration and derived equations related to the displacement of the soil skeleton and pore water pressure and other explanations can be found in Di and Sato [37].

Combining Eqs. (30) and (31) yields:

$$\dot{p}_w = \frac{K_w}{n} tr \left(\frac{\partial v_w}{\partial x} \right) \tag{32}$$

Assuming that the soil particles are incompressible, the porosity variation in each step can be calculated by the following equation [37]:

$$n^{t+dt} = 1 - \frac{1 - n^t}{J} \tag{33}$$

where J is the Jacobian determinant of the deformation gradient tensor.

Thus, the porosity is updated in every step according to the displacement of soil particles, and based on that, the pore water pressure is updated.

Like other numerical methods, modeling boundary conditions is one of the most essential steps affecting analysis results, especially in areas adjacent to rigid walls. Most of the problems reported from this perspective in SPH-based modeling mainly involve penetration of the particles within the boundaries and the kernel truncation at the borders [39].

The dynamic boundary particle technique was used in this study to apply the boundary conditions of physical models. Based on this technique, the dynamic boundary particles of the model are involved in all the SPH calculations, but they are fixed in place; hence, implying that position and velocity calculations do not apply to the boundary particles at each updated time step. Actually, the boundary particles in this method are like any other free particles with the difference that they are not allowed to move.

In the framework of this technique, the boundary particles of the models simulated in this study were defined using parallel layers of fixed particles. The number of layers required to prevent the kernel support truncation of free particles near the boundaries depends on the kernel type. In all the simulations performed in this study, two layers of boundary particles were selected, and the stability of the free particles was ensured. In addition, the no-slip boundary conditions in this study were applied to the rigid boundaries of the models based on the approach proposed by Bui et al. [31]. These procedures were performed separately for both soil and water particles.

In order to ensure numerical stability during the simulation process, the time step must be chosen according to the following criterion [26]:

$$\Delta t \leq 0.25 \min \left(\sqrt{h/a_i} \right) \quad (34)$$

where h is the smoothing length and a_i is the acceleration of the particle i .

Time stepping in this study is performed using the Verlet scheme of Monaghan [26] to integrate the continuity and momentum equations. It is noteworthy that the coefficient of 0.25, used in Eq. (34), is suitable for single-phase simulations [33], and due to the presence of interaction forces between water and soil in this study, by performing several simulations, a coefficient of 0.01 was placed in the equation to achieve numerical stability.

3 Numerical simulation of physical model tests

In this study, a series of large-scale laboratory model tests were performed to evaluate and validate the developed SPH code. These model experiments were designed to induce vertical and lateral displacements and large soil deformations during the shakings. In the following, the results of these tests, along with the simulation outputs, are presented and compared.

3.1 Water dam break simulation

Before applying a numerical simulation for model tests, the code should be verified for the reproduction of experimental data sets or exact results from other methods for benchmark problems. The water dam break simulation is a standard classic example typically employed to demonstrate the ability of the codes based on Lagrangian formulations of fluid flow problems [40–42].

For this purpose, the well-known dam break experimental test results have been used [43] to verify the simulation results of the SPH code through the present study. The authors of that study have entirely and accurately made the data related to the dam break test available to the public. This data can be downloaded from <http://canal.etsin.upm.es/papers/lobovskiyetaljfs2014/>.

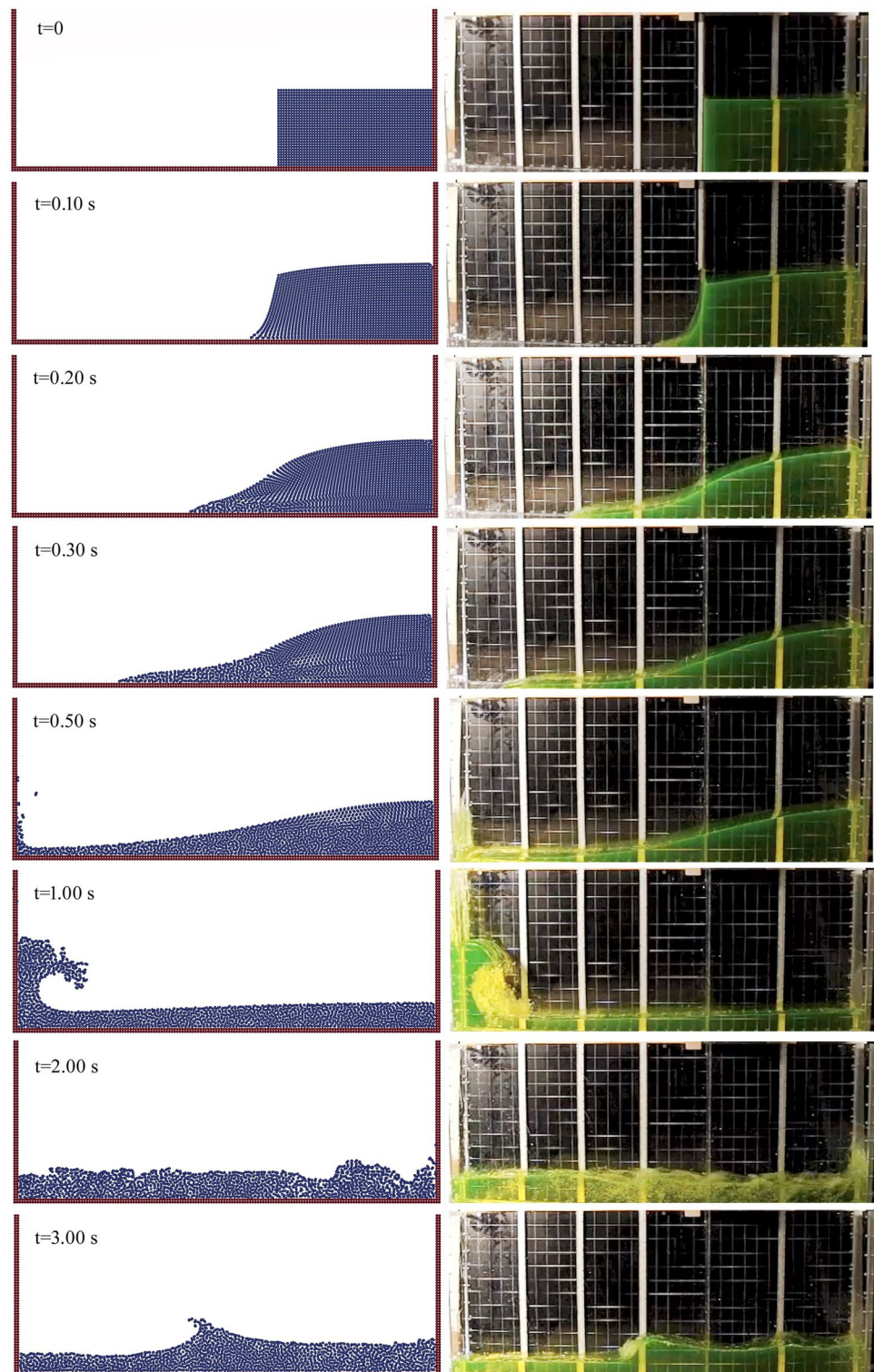
In the present study, the particles representing the water phase are simulated in the SPH analyses as a slightly compressible viscous fluid considering the Weakly Compressible SPH (WCSPH) approach [26]. The water column with an initial height and width of 0.30 m and 0.60 m, respectively, is retained by a removable gate, and as it is drawn up rapidly, the water column will start flowing along with the tank. More details about the specifications of the various components of the model, such as container, gate, etc., and experimental setup can be found in [43]. The fluid characteristic parameters and the details of particle modeling used in the simulation in this study are given in Table 1.

Figure 2 shows a 2-D side view of the water profile change along with the tank at different times. In addition, the simulation results by SPH at times corresponding to the

Table 1 Fluid particles characteristics used in the SPH simulations

Parameter	Value	Unit
Density of water	997	Kg/m ³
Dynamic viscosity	1×10^{-3}	N m ⁻² s
Speed of sound in water	55	m/s
Diameter of particles	0.01	m
Number of particles	1450	–

Fig. 2 Water dam break experimental and SPH-simulated results at various times



physical model are also given in this figure. As the comparison shows, there is a close conformity in terms of the fluid's free surface profile between the simulation results and the experimental model snapshots at different times and positions. As Fig. 2 bears witness, this consistency of the results can be observed in different prominent situations, including

shortly after release ($t=0.10$ s), where inertia forces dominated and gravitational acceleration caused the fluid to flow; the time after the water column collapsed and hit the left wall of the tank ($t=0.5$ s); the time when water tries to fall back in the opposite direction under the influence of gravity and impact energy ($t=1.0$ s); and the time when the wave

caused by backward movement after hitting the right wall ($t = 3.0$ s).

3.2 Vertical settlement of saturated sand

As part of this study, physical modeling of vertical settlement of saturated sand under seismic loading was conducted by some quick tank tests and compared with the simulation results of the SPH numerical modeling. These model tests were performed by a one-way excitations of sand models at different relative densities using a shaker provision, at the laboratory of soil mechanics at *University of Guilan*, to produce both liquefied and non-liquefied sand settlements.

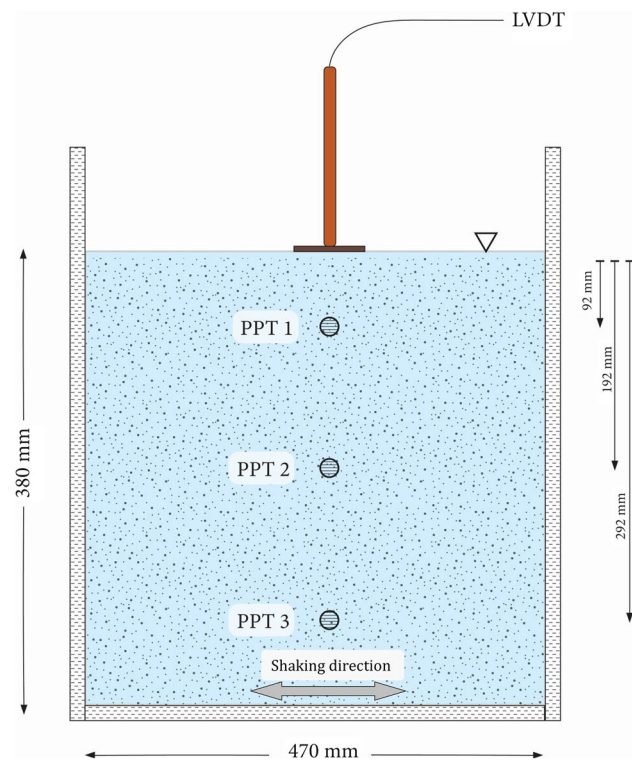


Fig. 3 General cross-section view of the quick tank model test and instrumentation details

The soil container with the internal dimensions of 47×47 cm and height of 58 cm made by 1.5 cm thick Plexi-glas walls is firmly bolted to the shaker. To reduce the shear wave reflecting effects of the sidewalls on the test results, foam sheets were used in the inner part of the two walls in the shaking direction. The water pressure transducers are located at three different depths (Fig. 3) to measure the excess pore water pressure (EPWP) during the test at the bottom, middle, and top of the soil deposit. Also, to continuously measure the vertical displacement (settlement) of the soil during the shakings, the average readings of the three linear variable differential transducer (LVDT) installed in different points of the surface of the soil profile were used. Further details about the quick tank used in the current research is provided by Jamshidi Chenari et al. [44]. Figure 4 shows a schematic view of the studied soil profile with the exact locations of the pore water pressure transducers.

The quick tank setup consists of various units and equipment, including electro-motors and components related to the horizontal reciprocal force creation, soil container and its supporting frame, pore water pressure and displacement transducers, and data recording and display devices. Figure 4 shows a bird's eye view of the one-way quick tank setup used in this part of the study.

In all the physical modeling experiments performed in the present study, the soil used was fine-grained sand, prepared

Table 2 Specifications of Anzali sand based on laboratory tests

Property	Designation	Value
Unified soil classification	USCS	SP
Effective particle size	D_{10}	0.10 mm
Mean particle size	D_{50}	0.34 mm
Uniformity coefficient	C_u	1.80
Coefficient of curvature	C_c	0.90
Specific gravity	G_s	2.67
Minimum void ratio	e_{min}	0.55
Maximum void ratio	e_{max}	0.88

Fig. 4 One-way quick tank setup and related equipment (left) and location of the pore water pressure transducers in soil container (right)



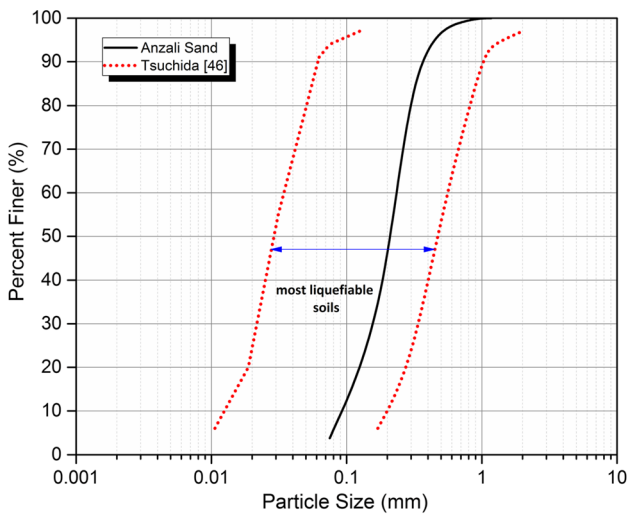


Fig. 5 Grain size distribution curve for Anzali sand

from the coast of Anzali, located in the southern part of the Caspian Sea in northern Iran. This sand is mainly composed of silica according to the microscopic digital images reported by Ahmadi et al. [45], and it exists in the form of sub-rounded particles. The main characteristics of the Anzali sand obtained from the laboratory tests are shown in Table 2.

The results of several studies have shown that most of the soils in this area have a high liquefaction potential due to their fine grains and full saturation [45]. This fact can be seen from the grain size distribution diagram of the sand used in this study (Fig. 5). This diagram also includes the grain size range of liquefaction-prone soils suggested by Tsuchida [46].

The sample preparation in all the experiments in this study was performed by the water sedimentation method. According to this method, oven-dried sand was continuously pluviated into the water so that the sand-fall height always remained constant relative to the water surface. Thus, uniform deposits with the desired relative density (D_r) were

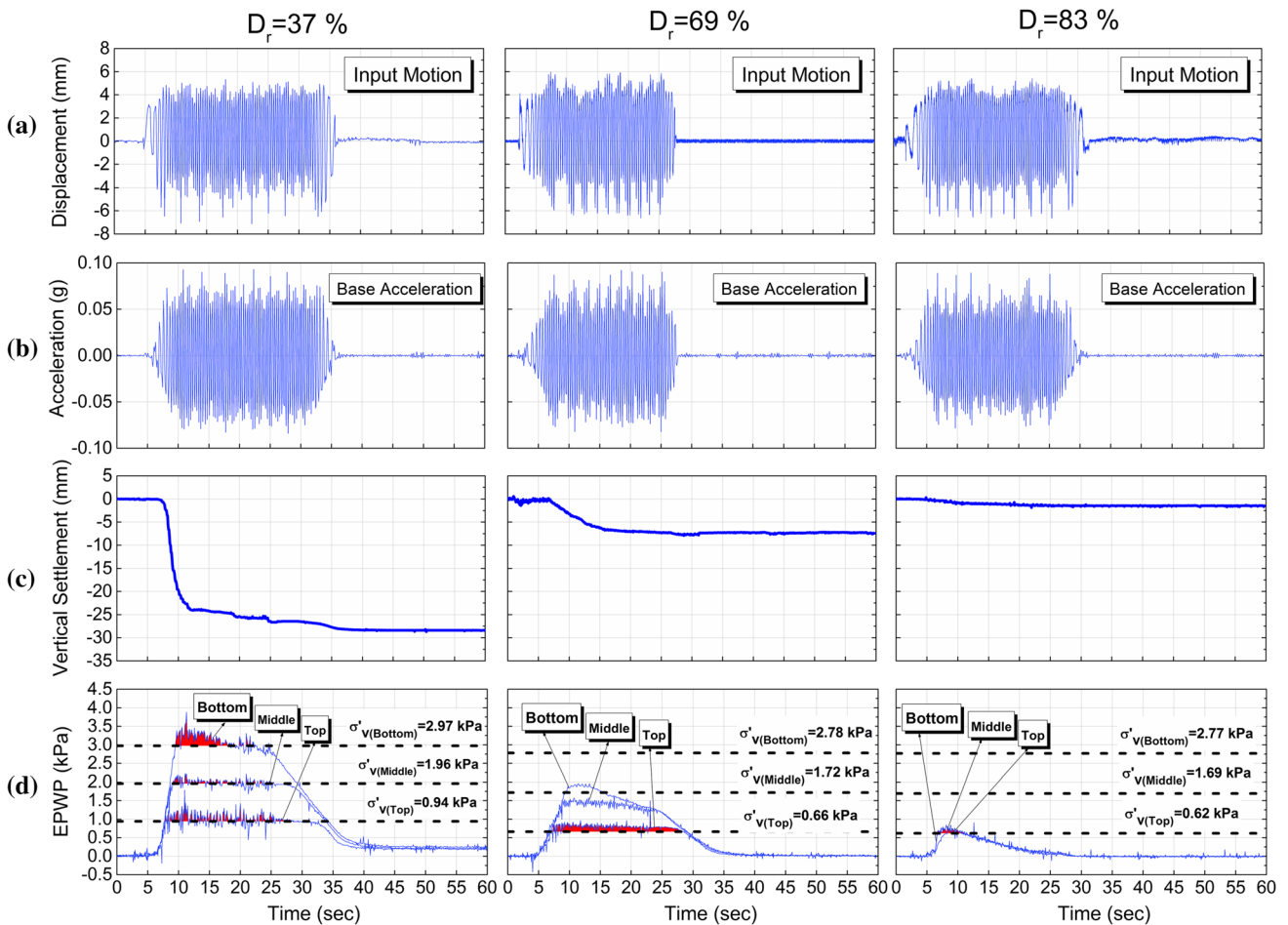


Fig. 6 Quick tank tests results for different relative densities; **a** input motion; **b** input acceleration; **c** vertical settlement; **d** excess pore water pressure (the areas highlighted in red indicate the occurrence of soil liquefaction)

obtained by controlling the height of the sand fall and, if necessary, applying small shocks. In this study, three relative densities of 37, 69, and 83% were used for physical and numerical modeling of the liquefaction-induced settlement of uniform sand under seismic loading.

Figure 6 shows the quick tank tests results for vertical settlement and excess pore water pressure (EPWP) in three different relative densities. The relative density of the deposited sand was varied through different tests, while other important parameters such as the excitation frequency, input motion amplitude, and the shaking duration was maintained constant. From Fig. 6, the motion (Fig. 6a) and acceleration (Fig. 6b) amplitudes are about 8 mm and 0.1 g, respectively, at a shaking duration of round 25 s for all three experiments.

The vertical settlement of the soil for tests with different relative densities is shown in Fig. 6c. In these tests, the ultimate cumulative settlements of 30, 8, and 1.5 mm were recorded at corresponding relative densities of 37, 69, and 83%, respectively. Moreover, pore water pressure time histories at the bottom, middle, and top of the models of different relative densities are presented in Fig. 6d. It is evident from different illustrations that, for loose soil ($D_r=37\%$), the excess pore water pressure level is significantly higher than other density states at three different elevations. It is also worth noting that the difference between the induced excess pore water pressure values at different elevations diminishes as the soil density increases.

Superimposed on the plots of the excess pore water pressure (Fig. 6d) are the lines corresponding to the effective stress values at different elevations in the form of dashed lines. The areas in the diagram where the excess pore water pressure exceeded the initial effective stress of soil are highlighted in red to show the soil liquefaction at different depths of the models. It can be seen that in the loose sand model, the soil liquefaction occurred in all depths. However, in the medium dense model, liquefaction has occurred solely at shallower depths, and in the dense sand, almost no liquefaction is observed. From a grain-scale perspective, this can be attributed to the formation of different force chains at different soil densities. Clearly, as the contact force between the particles increases, either due to the increase in depth or through higher density, the force chain network becomes stronger between the particles. As a result, in higher-density specimens, due to larger force chains and consequently stronger inter-particle contacts, the potential for dynamic shear strength loss and liquefaction of the soil is significantly reduced.

Simultaneous review of acceleration, settlement, and excess pore water pressure histories is also important. In the loose sand model, where the soil is liquefied throughout the deposit, most of the settlement occurs at early shaking stage and is concurrent with the onset of liquefaction. In this case, the soil settlement continues even after the shaking

ceases and accumulates up to 7% of the total settlement. On the contrary, in moderate and especially dense models, settlements increased approximately linearly with the time of shaking, and no more settlements occurred after the end of the earthquake.

The quick tank tests are simulated as a 2-D plane strain problem in the developed SPH code. In this regard, soil and water are modeled as a series of single particles in separate phases. In total, the model was simulated using 4416 soil and water particles. A detailed description of the constitutive model used for the soil and equations of state for water was provided earlier in Sect. 2. Furthermore, a no-slip boundary condition is applied for solid walls.

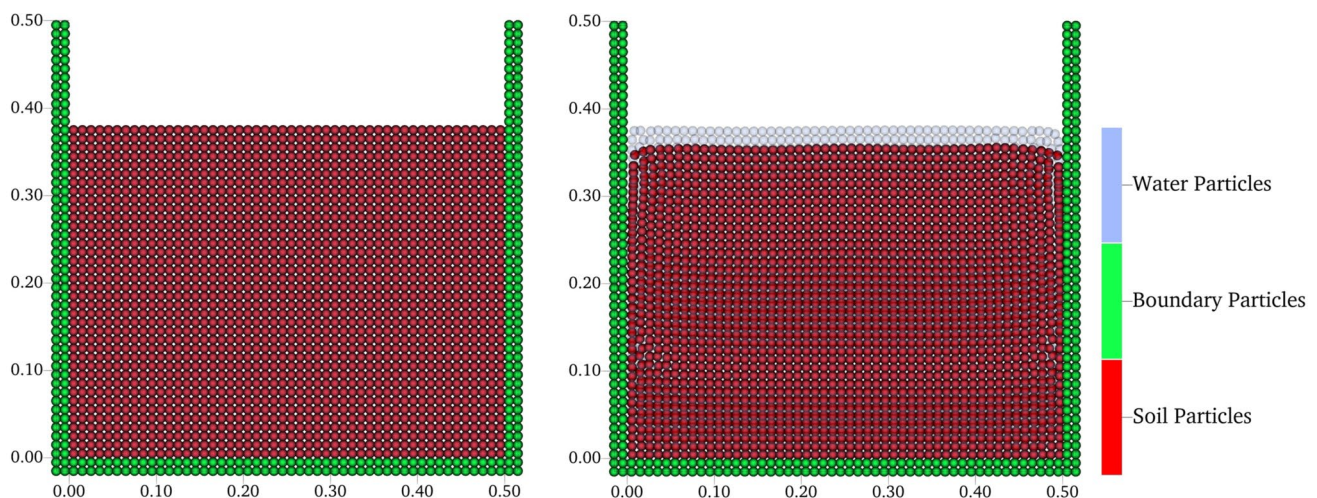
A summary of these parameters is listed in Table 3 for the simulated models with different relative densities. An important point to note about the soil parameters given in Table 3 is that these parameters (in particular, the parameters related to the soil strength characteristics such as Young's modulus, Poisson's ratio, internal friction angle, and cohesion) are directly derived from laboratory triaxial tests on the samples. Thus, it represents the values of these parameters at the macroscopic scale of the soil samples and does not contribute to the grain-size parameters as suggested by Sandeep and Senetakis [47] and Sandeep et al. [48] for micromechanical behavior of soil.

Figure 7 shows an overview of the initial SPH model and the arrangement of the particles simulated (left view). As mentioned before, soil and water particles were considered two separate phases in the simulations; the two types of particles are initially at the same pattern in terms of particle distance and orientation. The same initial position is assigned to soil and water particles. This figure also shows the particle arrangement for the loose sand model after applying the shaking (right view). As can be seen from this figure, vertical settlement of soil particles has occurred due to the induced motions by the walls and has become closer to each other in the water.

Numerical simulations of the quick tank tests for medium and dense sand were performed similarly to the procedure presented for loose sand. The vertical settlement time histories from the numerical simulations and the values from the quick tank experiments are shown in Fig. 8 for loose, medium, and dense sand samples. The numerically simulated vertical settlement diagrams shown in these figures are obtained by continuously plotting the average vertical displacement of the particles located on the middle of the soil surface over time. Comparison of experimental and simulation results shows that although in medium and dense samples, the ultimate settlements are slightly over-predicted, the simulated settlement generally follows a trend similar to the experimental model tests results. Also, the major settlement induced by liquefaction onset occurs relatively more quickly in the loose

Table 3 Parameters used in the SPH simulations of vertical settlement of saturated soil in different quick tank models

	Property	Unit	Symbol	Value		
				Loose	Medium	Dense
Soil	Saturated density	kg/m ³	ρ_s	1960	1978	2010
	Dry density	kg/m ³	ρ_d	1534	1564	1616
	Initial void ratio	–	e_0	0.739	0.705	0.653
	Young's modulus	kg/cm ²	E_s	85	140	185
	Poisson's ratio	–	ν_s	0.34	0.34	0.34
	Internal friction angle	Degree (°)	φ_s	25.0	25.0	25.0
	Cohesion	kPa	c	5	5	5
	Sound speed	m/s	C_s	67	88	100
	Particle spacing (size)	m	dx	0.01	0.01	0.01
	Smoothing length	M	h	0.012	0.012	0.012
Water	Density	kg/m ³	ρ_w	983		
	Dynamic viscosity	Pa.s	μ_w	0.00089		
	Sound speed	m/s	C_w	55		
	Initial time step	sec	Δt^0	0.0027		
	Bulk modulus	MPa	K_w	2050		
	Particle spacing (size)	m	dx	0.01		
	Smoothing length	m	h	0.012		

**Fig. 7** Numerical model of quick tank test simulated in the SPH code, initial particles arrangement (left) and vertical settlement occurred in saturated loose sand at the end of shaking (right)

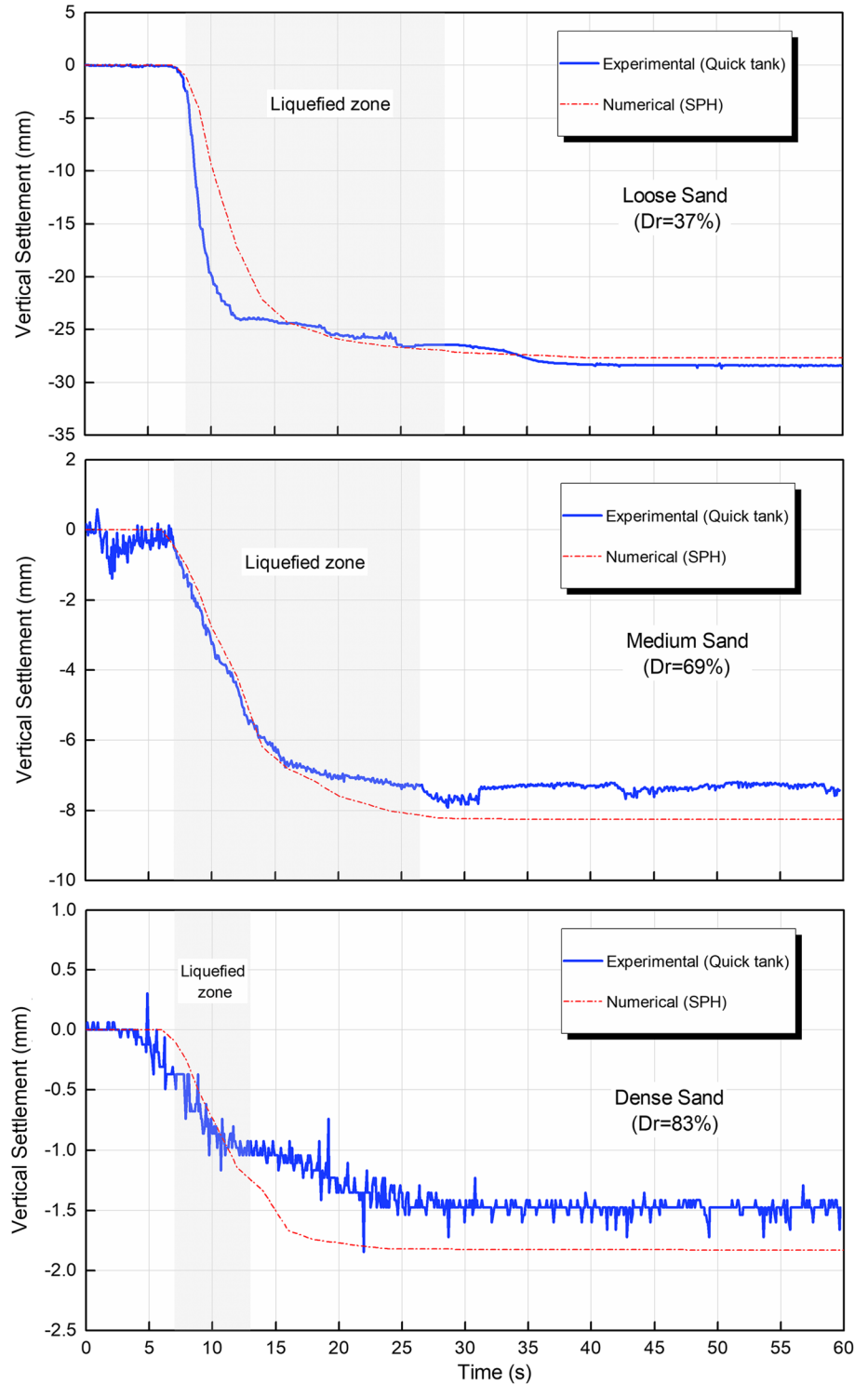
sand model than the other two cases. As mentioned in the experimental results section, in the simulation, the post-liquefaction settlement in the loose sample did not stop at the end of the shaking; it continued and stopped after an increase of about 4%.

As previously mentioned in Sect. 2, in this study, the pore water pressure and, consequently, the effective stress are obtained by considering the idea of variable porosity in the SPH formulation. In line with this two-phase framework, the stress in soil particles is obtained based on an elastic-perfectly plastic constitutive model. The pore water pressure

is calculated by considering soil–water interaction in terms of changes in porosity that are updated at every time step.

Here we investigate, for example, the simulated pore water pressure build-up and dissipation for the quick tank experiments for the loose sample. For the rest of the models, the outputs are presented as Supplementary Materials to this paper. The measured time histories of excess pore water pressure for this very experiment have already been shown in Fig. 6. The contour plots of the excess pore water pressure throughout the soil depth obtained from the simulations are shown in Fig. 9 for the loose sand model. These results

Fig. 8 Experimental vs. numerical results of vertical settlement of saturated sand for loose, medium, and dense models



are displayed for the times before the shaking (hydrostatic conditions), the onset of liquefaction, and the end of the shaking.

A more detailed analysis of the excess pore water pressure build-up and its dissipation can be performed by the time histories shown in Fig. 10 for the loose sand model at

the top, middle, and bottom points. In this figure, the excess pore water pressure values obtained from the simulation and those recorded in the quick tank experiments (previously shown in Fig. 6) are depicted. It is worth mentioning that the EPWP values obtained from the simulations are

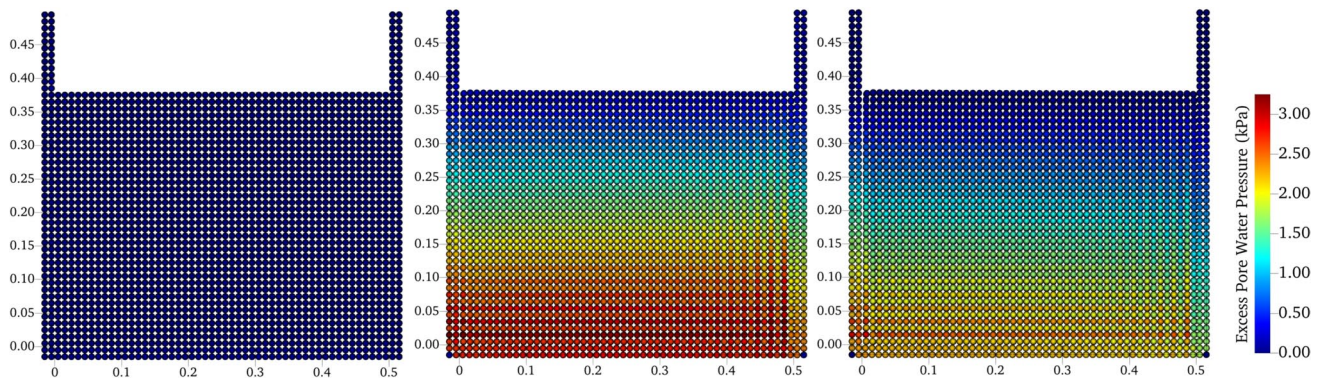


Fig. 9 Excess pore water pressure obtained by simulation of the loose sand quick tank model for the times of pre-shaking (left), the onset of liquefaction (middle), and the end of shaking (right)

the time-marching outputs for water particles located at the points shown in Fig. 3.

The SPH-simulated EPWP diagrams in Fig. 10 show that, as recorded in the physical model tests, the excess pore water pressure increases to a maximum value under the dynamic excitation induced by the shakings. This maximum value for all the control points occurs approximately at the onset of liquefaction. The simulated pore water pressure values are in a relatively acceptable level of agreement with the experimental ones in build-up and persistence during the shaking and liquefaction occurrence. However, after shaking, contrary to what was observed in the physical modeling tests, the residual excess pore water pressure does not decrease significantly and dissipates longer than the experimental results. This may be attributed to the post-liquefaction fate of sand particles, such as the void redistribution phenomenon in which the soil and water particles move within a zone of constant overall volume (end of soil settlement) and the localized void ratio in the soil deposit [49]. Therefore, considering this effect is essential in improving the void ratio calculations and consequently more accurate estimation of the post-liquefaction pore water pressure dissipation and can be the focus of future complementary research in this field.

3.3 Lateral spreading and large deformation of liquefied sand

This section investigates the results of a shaking table model test on liquefaction-induced large lateral deformations of saturated sand compared with simulation results from the SPH-developed code. The soil used in this experiment is Anzali sand with the same characteristics used in the previous quick tank experiments. The shaking table machine deployed in this study is a uniaxial table with a foot print of 1000×1000 mm, shaken by a digitally controlled servo-electric actuator and fabricated at University of Guilan. Detailed description of the specification of this very shaking

table is provided elsewhere [50–52]. It provides the ability to place model boxes with larger dimensions to perform tests with larger-scale soil models. In fact, to observe the large soil deformations during and after the shaking process, a different transparent plexiglass box was designed and built with a larger length than the vertical settlement test setup. The soil box has internal dimensions of $900 \times 500 \times 500$ mm in length, width, and height, respectively. Also, plexiglass walls have been used to easily monitor and track the soil deformations and failure progress.

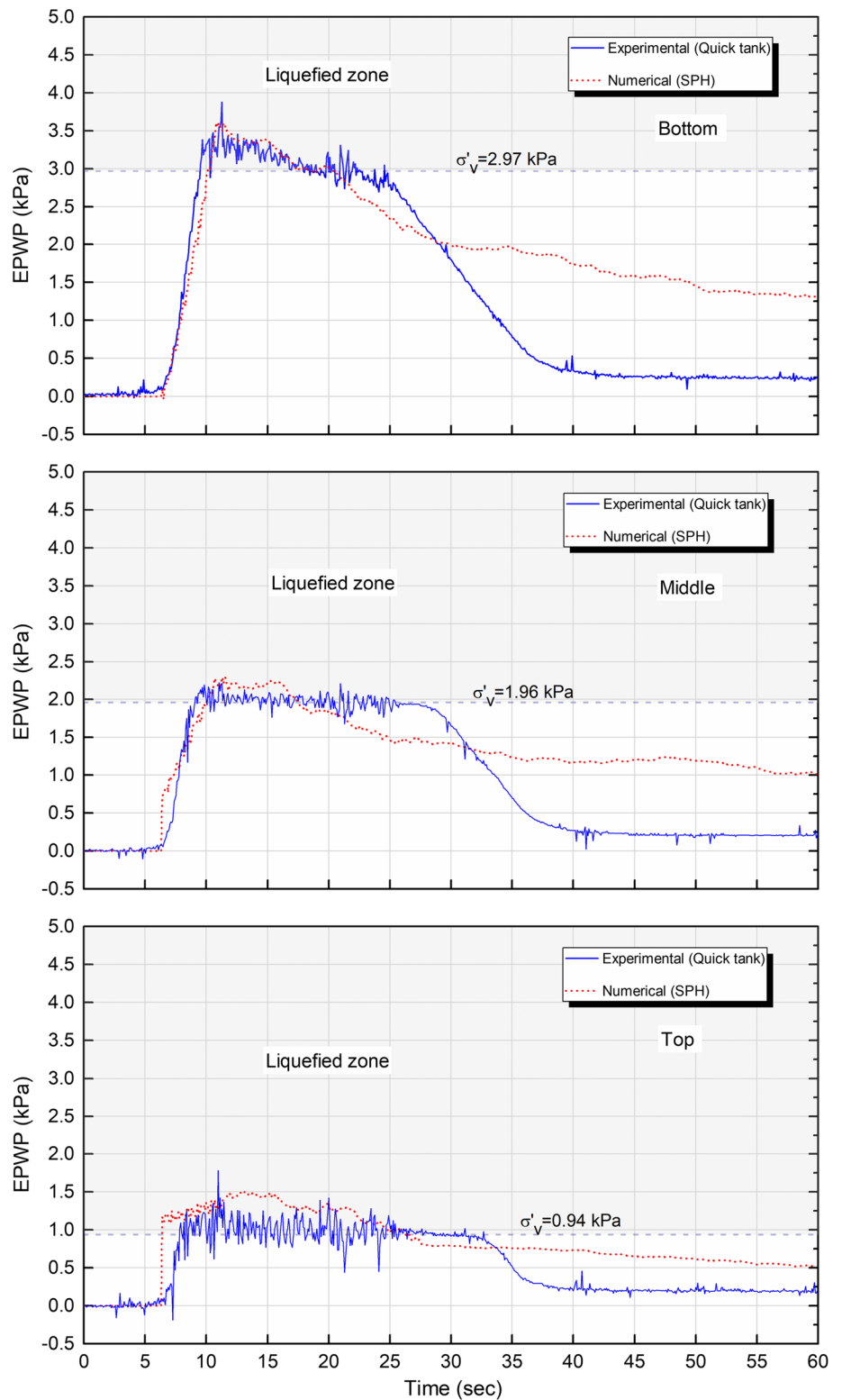
A view of the shaking table apparatus used in this test and its associated equipment is shown in Fig. 11, and further specifications and details of the transparent plexiglass box and respective equipment are described in [52].

The excess pore water pressure (EPWP) build-up and dissipation measurement in this test was carried out by two pressure transducers fixed firmly to the box wall at one-third and two-thirds of the height of the box.

Unlike the quick tank model tests, in which settlement was measured at the soil surface using LVDTs, in this test, due to the shaking-induced large deformations, both vertically and horizontally, the continuous capturing method was resorted instead of LVDT measurements. This method used a high-speed video camera at a fixed location, and the soil body movements were continuously recorded. Then using a software for motion tracking, it was possible to analyze the lateral large deformation and failure of the liquefied soil at any given time.

The sample preparation was performed in a fashion similar to the quick sand tests by the water sedimentation method. Using this method, the model with the desired geometry and a relative density of 38% was obtained. Figure 12 shows a schematic view of the shaking table model test setup. The results of soil deformation analysis in this section will be presented for the three different points shown in the positions near the slope (B1), on the slope (D1), and near the slope toe (G1).

Fig. 10 Measured versus simulated excess pore water pressure time histories for the points located at the bottom, middle, and top of the loose sand model in the quick tank



To study the soil behavior before, during, and after liquefaction, some preliminary tests were performed to determine the required frequency and duration of shaking. Accordingly, a harmonic input motion with an amplitude of about 2 mm was applied to the model at a frequency of 6 Hz. Also, the

shaking amplitude was selected so that no significant deformation would occur in the model before the soil liquefaction. The induced shaking was maintained for 20 s and then terminated. The measurements, however, continued for up to 40 s after the end of shaking.

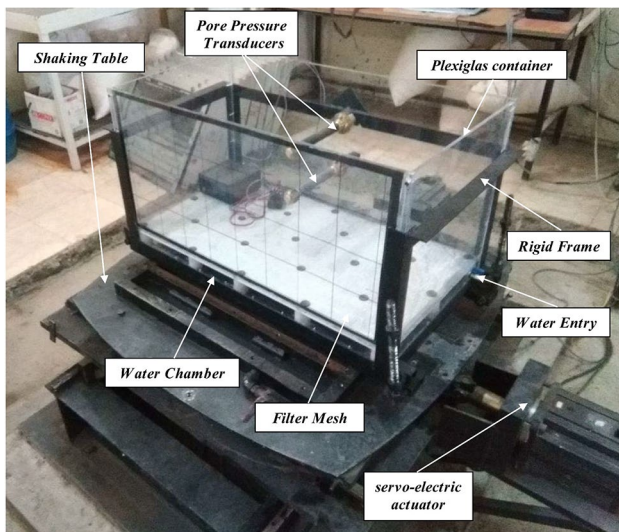


Fig. 11 Shaking table and transparent soil box used for large deformation analysis in this study

The time history of the input motion applied to the model has been shown in Fig. 13a. The input acceleration is obtained by double differentiation of the input motion time history, as shown in Fig. 13b. It can be seen from this figure that the maximum input acceleration (a_{max}) is about 0.6 g.

All deformation profiles related to the shaking table test presented in this section have been obtained by tracking pre-embedded colored lines in the soil. Thus, it is possible to get the continuous deformation time history at any desired point.

To evaluate the simulation capability of the developed SPH code, the same geometry as tested in the shaking table machine was numerically simulated. As in the quick tank (vertical settlement) simulations in previous sections, water and soil medium are modeled as separate phases. A total of 4607 soil and water particles were created with the

specifications listed in Table 3. Also, a no-slip boundary condition is adopted for the solid walls of the model. A harmonic reciprocating motion with an amplitude of 2 mm and a duration of 20 s was also applied to the model walls to simulate the input motion used in the shaking table test.

The configuration and deformation of the simulated model at different times are shown in Fig. 14 along with the pictures from the shaking table experiments. From Fig. 14, it can generally be seen that the soil failure occurred in the model due to shaking and liquefaction, the flowing mass moved downstream, and soil particles have accumulated around the toe due to volume transfer from the upstream.

Figure 15 also shows the final geometry of the model based on the deformations resulting from the numerical simulation by SPH, along with the initial geometry of the model and the deformations recorded in the shaking table test.

Referring to Figs. 14 and 15, it can be clearly seen that the numerical simulation results by SPH almost agree with the experimental results. This agreement is more evident in the upstream of the model and in the downstream and the slope section. However, there is a slight difference in the predicted displacement values compared to the experimental results. From the authors' point of view, this difference may be attributed to two facts: first, the soil parameters used in the constitutive model in the simulation, such as internal friction angle, cohesion, elastic modulus, etc., have been obtained from laboratory tests and may differ from the in-situ values in the 1 g shaking table test; second, in numerical simulations, it is assumed that the main parameters determining soil behavior remain constant during the test, which may not reflect the actual in-situ experimental conditions. These cases can be improved by using more advanced soil constitutive models to update the constitutive parameters as shaking-induced deformation develops through time.

Figure 16 shows the contour plot of the horizontal displacement that occurred in the model at the end of the

Fig. 12 The model test configuration used in large deformation analysis by shaking table experiments

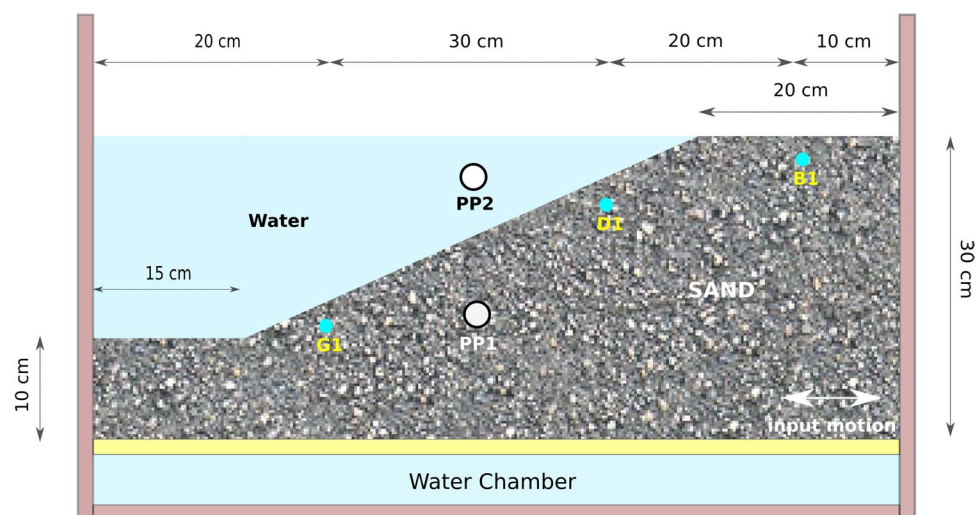
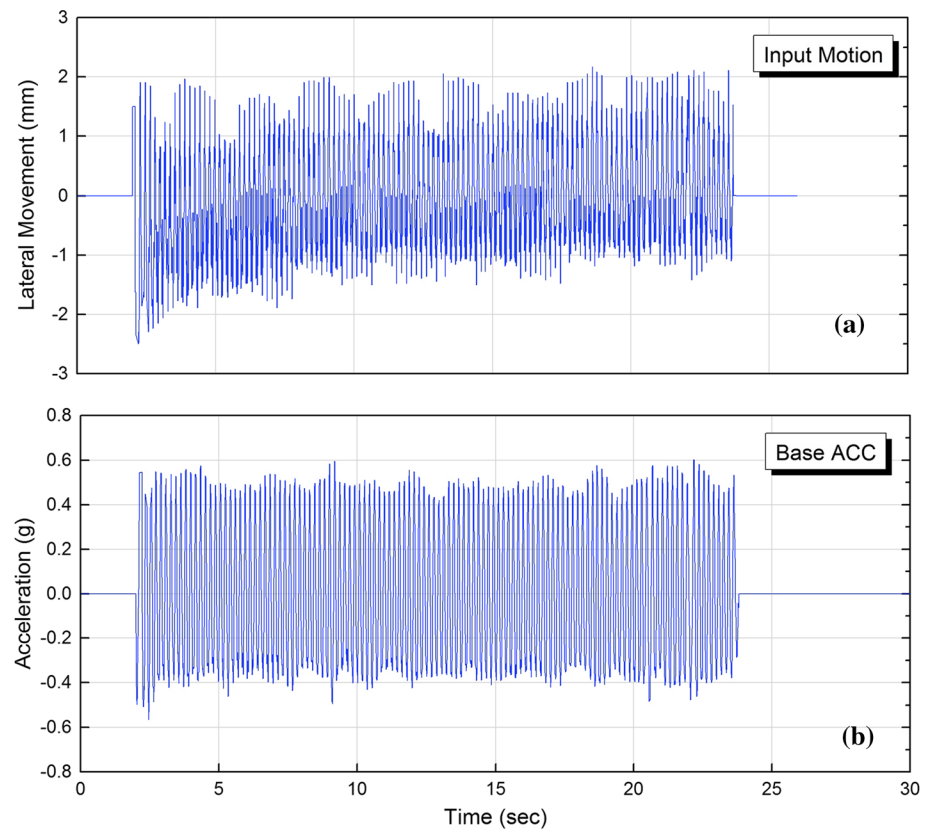


Fig. 13 Time histories of the excitation applied to shaking table in the large deformation model; **a** input motion; and **b** derived input acceleration



shaking. As can be seen from this figure, most soil movements occurred at the top of the slope in the model. Another observed event is the absence of any distinct slip surface in form of a sliding block in the model.

In fact, due to the soil uniformity in the model and the absence of fine-grained layers, low-permeability interlayers, and thin lenses, soil failure extends in deeper levels and wider areas [53], resulting in the flow failure of the soil.

An overview of general model deformations at different times shows that most soil deformation occurs before the end of shaking. After that, while the deformation continues, no significant displacements occur in the model. This is attributed to the pore water pressure build-up and dissipation mechanism during soil liquefaction and can be seen in more details in Fig. 17. In this figure, the excess pore water pressure changes recorded by the pore pressure transducer in the soil layer (PP1 in Fig. 12) have been displayed over time along with the SPH numerical simulation results. In addition, the effective stress at this point is calculated and shown as a dashed line in the diagram, with the gray zone representing the liquefaction occurrence potential.

As can be seen, the excess pore water pressure increases progressively after the shaking starts, and after about 5 s, it reaches the effective soil stress, which means that the soil liquefies. Soil liquefaction lasts for more than 5 s and then ends with the EPWP dissipation while the shaking

continues. The EPWP dissipation is per se imputable to the rapid drainage of the pore water during the soil dilation. Although, the complete dissipation of the excess pore water pressure takes longer.

The SPH simulated EPWP time history is also superimposed on Fig. 17 for comparison purpose. This data results from the continuous output of the numerically simulated pressure of the water particle located at the point corresponding to the measurement spot. It can be stated that the pattern of the excess pore water pressure build-up and dissipation approximately follows the experimental trend. However, there is a slight difference in the onset of liquefaction and the duration of this phenomenon in the numerical solution. In addition, as discussed earlier in regards with the simulations of the vertical settlement, here too, after the shaking is over, the simulated EPWP is dissipated more slowly than the experimental results do. This was stated earlier to be imputable to the inadequacy of current formulations embedded in the adopted SPH method for the void ratio evolution and calculations, which is left for further refinement.

Pore water pressure, as an important factor in determining the liquefaction, is closely related to the energy dissipated during cyclic loading. This has been the focus of many studies in the last four decades [54–59]. According to the principle of energy dissipation, the amount of dissipated energy in each cycle of dynamic loading can be calculated through the

Fig. 14 Model deformations at different times for shaking table test (right) and numerical simulations by SPH

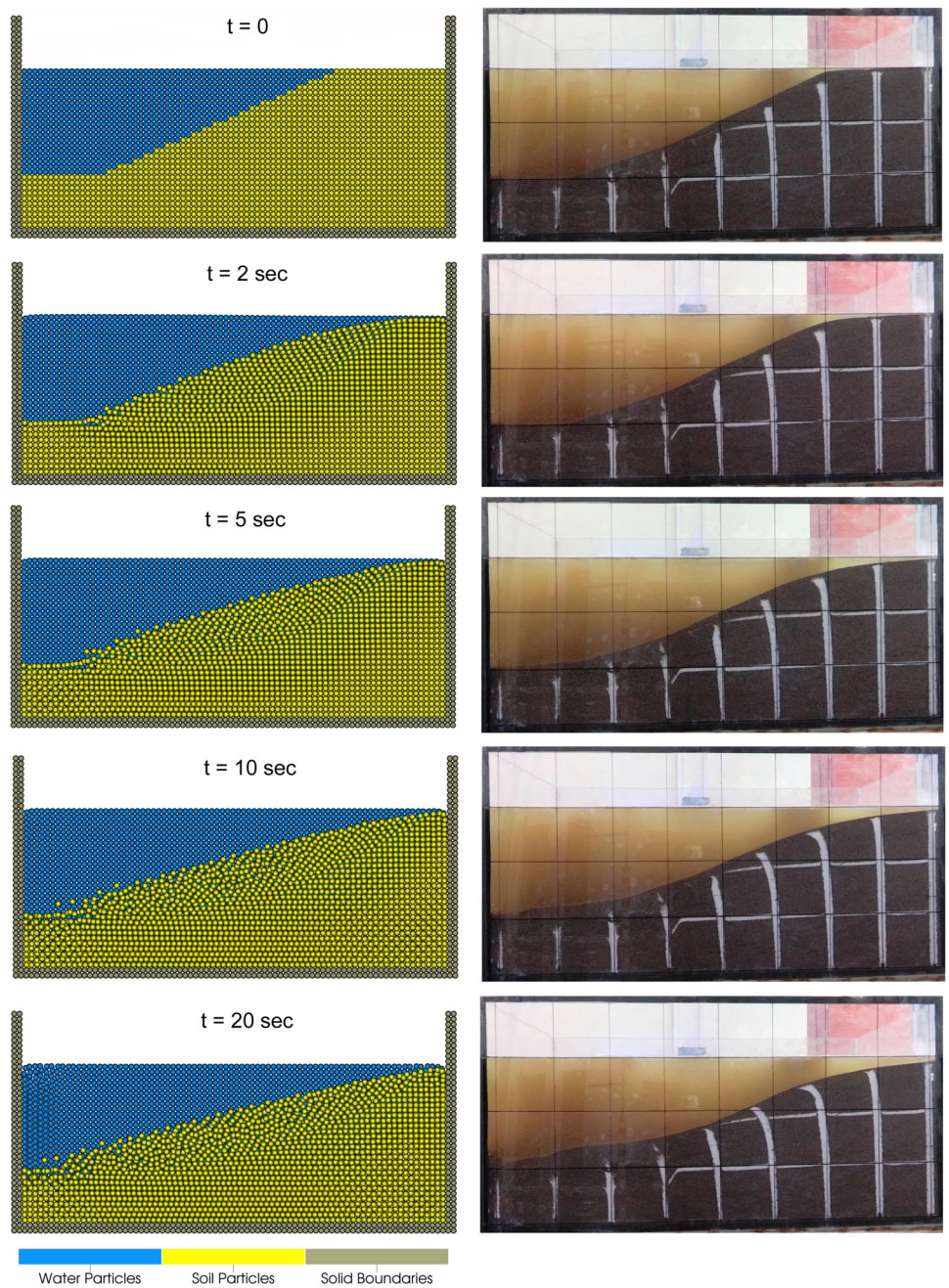


Fig. 15 Comparison of final deformed shape of the model for shaking table test and SPH numerical simulation

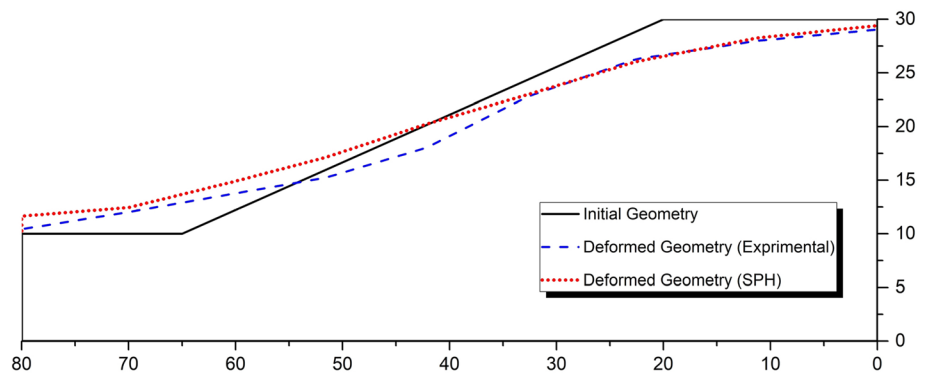


Fig. 16 Contour plot of the horizontal displacement at the end of shaking table test

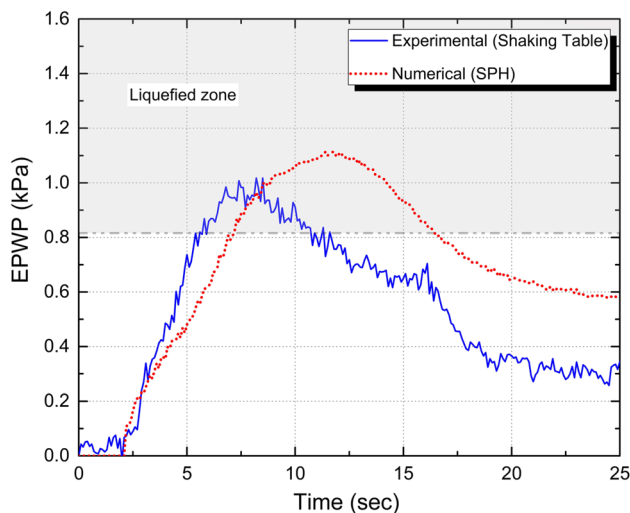
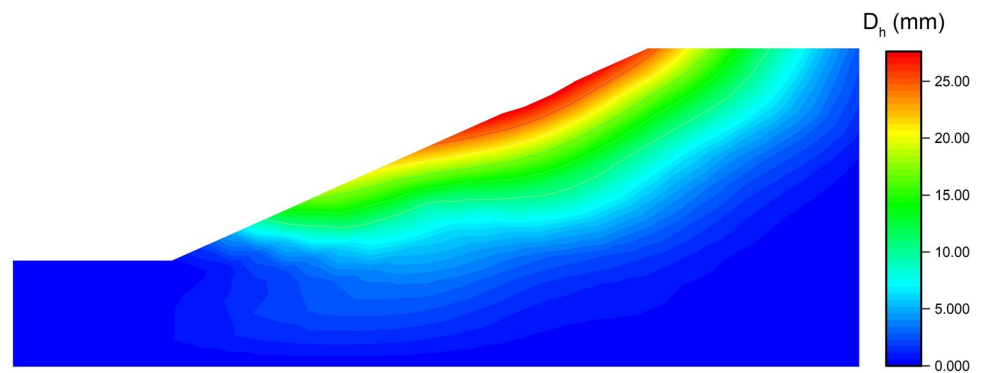


Fig. 17 Time histories of the excess pore water pressure at the point PP1 in the shaking table model test and SPH simulation

area enclosed by the hysteresis loop of a shear stress–strain curve. In this study, the shear stress and strain time histories were calculated at point PP1 in the shaking table test (as shown in Fig. 12) using the acceleration records based on the method presented by Zeghal and Elgamal [60]. Accordingly, the equations of for shear stress and strain were calculated using the acceleration and lateral displacement records. A more complete explanations for obtaining equations along with calculations related to the dissipated energy in each cycle can be found in Jamshidi Chenari et al. [61]. Applying the above-mentioned approach, the shear stress–strain diagram is shown in Fig. 18a for the point corresponding to where the pore water pressure was measured, PP1. As can be seen in this figure, a deviation from the regular pattern of hysteresis loops obtained for laboratory element-size tests is observed, representing the dilative response behavior of liquefied sand at large cyclic shear strains in the form of strain-hardening shear stress spikes. A similar shear-strain behavior for a sloping soil modeled in a centrifuge model

undergoing large strains has been reported by Taboada and Dobry [62].

By calculating the energy per unit volume (energy density) dissipated in one cycle of dynamic loading through the shear stress–strain curve, the diagrams of changes in energy dissipation per cycle and total accumulated energy over time are shown in Fig. 18b, c, respectively. Also, for simultaneous comparison, the excess pore water pressure variations are plotted in Fig. 18d. As shown in Fig. 18b, the maximum amount of dissipated energy per cycle occurs when the excess pore water pressure was at its maximum value. In other words, the most significant amount of energy dissipation occurs during the period from the onset of liquefaction to the beginning of pore water pressure dissipation. After that, we see smaller amounts of energy dissipation, although this energy dissipation does not reach zero because of what was explained about the dilative behavior and strain-hardening at large strains regimes. A similar conclusion can be drawn about the variations of total accumulated energy in Fig. 18c, in which the rate of increase in total accumulated energy is higher until the soil liquefies, and then this rate decreases.

Figure 18e illustrates a scattered plot of variations in dissipated energy per cycle versus excess pore water pressure ratio (r_u) at point PP1 in shaking table test. Similarly, this diagram shows an increasing trend of dissipated energy with increasing pore water pressure, which confirms the previously mentioned results.

Considering the particles located at points B1, D1, and G1 (previously defined in Fig. 12) for analysis in the shaking table test and simulated model, the time histories of the horizontal displacement are obtained and shown in Fig. 19.

As can be seen in these figures, there is a fairly good agreement between the SPH numerical simulation results and the experimental data. The SPH simulation, except for the point located on the slope (D1), slightly over-predicted the horizontal displacements. A noteworthy point in the results of numerical simulations and experimental records is the horizontal displacement rate that occurred during the progress of the experiment. For points B1 and D1, most

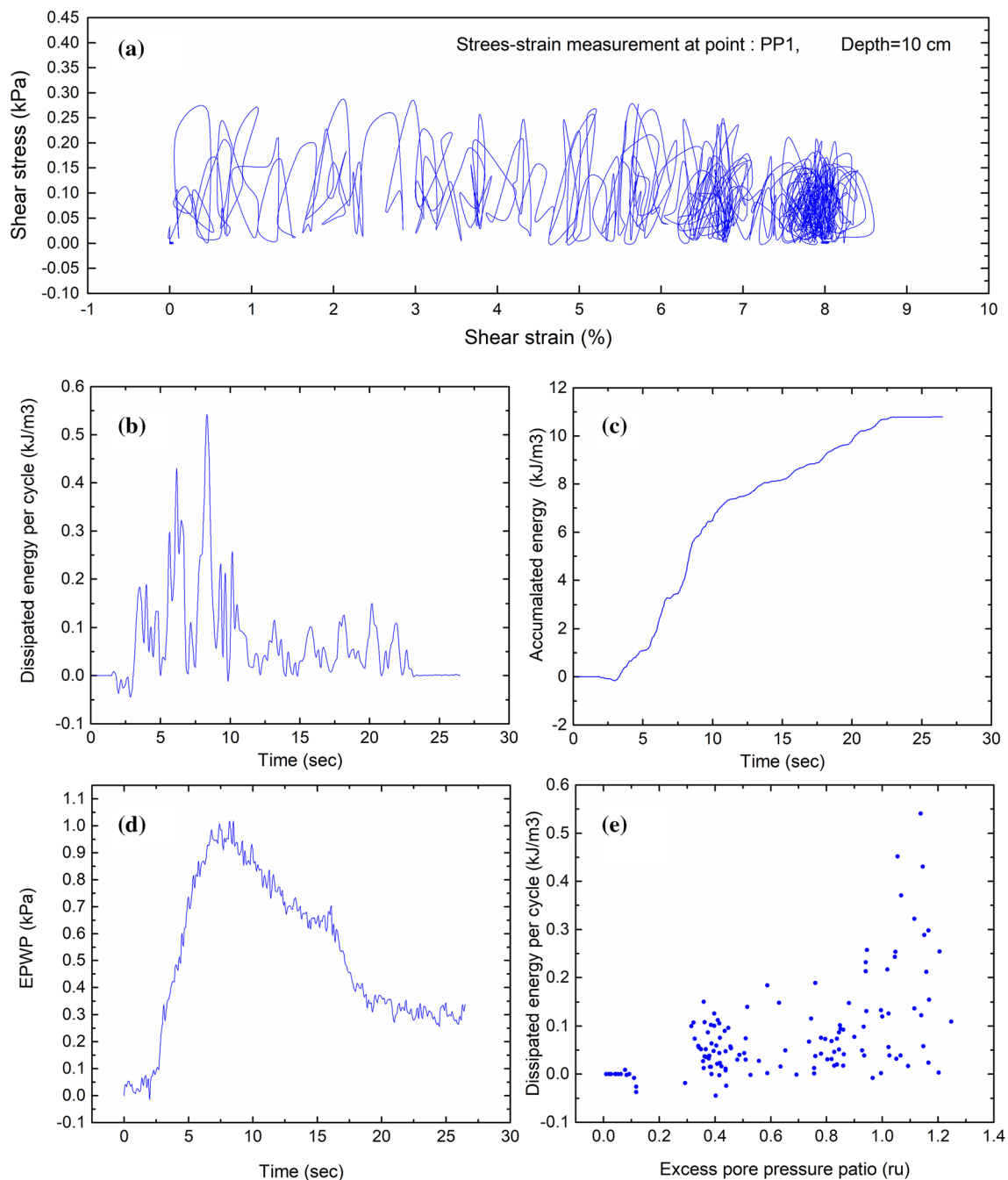


Fig. 18 Comparison of different diagrams obtained from shaking table test results for point PP1 (shown in Fig. 12); **a** shear stress-strain history; **b** energy per unit volume dissipated during each cycle;

c cumulative energy per unit volume dissipated after each cycle; **d** excess pore water pressure time history; **e** attenuated energy corresponding to the pore water pressure ratio

of the cumulative horizontal displacement resulting from the simulation occurs approximately 10 s after the start of the shaking, after which there is no significant increase in displacements. For the results recorded in the experimental experiment, this time is slightly different and takes a little longer. Contrary to these two points, the horizontal

displacement at the point G1 gradually increased and continued until the end of the shaking. Given the location of this point at the downstream, this can be attributed to the induced forces caused by the accumulation of the particles moving from the upstream, regardless of the liquefaction effect.

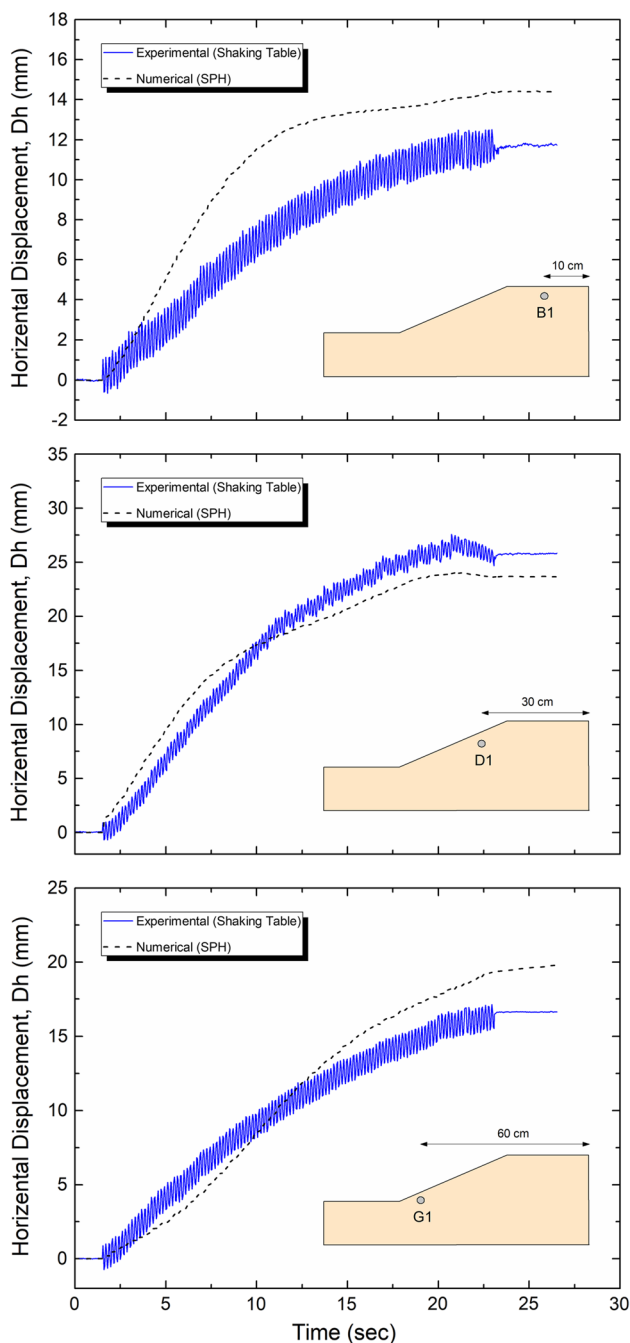


Fig. 19 Time histories of horizontal soil displacements for shaking table model test and SPH simulation at different locations

4 Conclusions

This study used the smoothed particle hydrodynamic (SPH) method to simulate vertical and lateral liquefaction-induced displacements. An elastic-perfectly plastic constitutive model was used to model the motion of soil particles. The idea of variable porosity was also included in the

formulations to more accurately simulate the pore water pressure during the large deformation of soil as shaking progressed. The results were compared with the data from experimental tests on different physical model tests.

In both sections of the vertical settlement and lateral displacement investigations, it was shown that the displacement results of the numerical simulation by SPH are in relatively good agreement with the experimental data. However, the SPH simulation results slightly overestimated the experimental results.

In addition, the excess pore water pressure build-up and dissipation were also investigated as an essential factor in the occurrence of vertical and lateral displacements due to soil liquefaction during the shaking. The study of the effect of pore water pressure in the shaker test results showed that the majority of dynamically vertical soil settlements in all three different densities of loose, medium and dense occurs when the excess pore water pressure is maximum values has led to liquefaction. The role of excess pore water pressure was also investigated in the shaking table test and it was found that the most of the lateral displacement of the model occurred during the period of liquefaction. A similar conclusion was also obtained in the numerical simulations of the experiments by the developed SPH code. Comparison of numerical simulation results and experimental values showed that the trend of build-up and development of the excess pore water pressure during the shaking was in good agreement with the results recorded by transducers in experimental tests. However, there was a difference between the simulated results and the experimental data in its dissipation after the shaking.

Also, the development of pore water pressure and initiation of liquefaction were investigated at different depths and densities of soil. In terms of micromechanical behavior, the liquefaction resistance due to the higher shear strength of the soil at higher depths and densities was attributed to greater inter-particle contact forces and, consequently, the formation of stronger force chains. However, this effect controls the macroscopic behavior of granular materials in conjunction with other grain-scale parameters, such as inter-particle friction and surface roughness.

In addition, the matter of energy dissipation during dynamic loading was investigated in the shaking table test by obtaining the shear stress–strain response of the soil from the acceleration and displacement data recorded in the test. Evaluation of the amount of dissipated energy and comparison by excess pore water pressure revealed a close correlation between these two parameters. It was concluded that the highest amount of energy dissipation coincides with the liquefaction occurrence.

Interpretation of the data obtained from this study suggests that due to the complexity of the liquefied-induced large deformation mechanism and the role of the excess pore

water pressure build-up and dissipation, the effect of various factors such as void redistribution, changes in soil parameters during the experiment, etc., should be considered in future studies to improve the simulation accuracy for this very phenomenon.

Supplementary Information The online version contains supplementary material available at <https://doi.org/10.1007/s10035-022-01267-x>.

Funding The authors would like to address that no funding was received to carry out this research.

Declarations

Conflict of interest The authors declare that they have no conflict of interest.

References

- Haiyang, Z., Jing, Y., Su, C., Hongxu, L., Kai, Z., Guoxing, C.: Liquefaction performance and deformation of slightly sloping site in floodplains of the lower reaches of Yangtze River. *Ocean Eng.* **217**, 107869 (2020)
- Mohammadnejad, T., Andrade, J.E.: Flow liquefaction instability prediction using finite elements. *Acta Geotech.* **10**, 83–100 (2015)
- Tamate, S., Towhata, I.: Numerical simulation of ground flow caused by seismic liquefaction. *Soil Dyn. Earthq. Eng.* **18**, 473–485 (1999)
- Beatty, M.H., Byrne, P.M.: Liquefaction and deformation analyses using a total stress approach. *J. Geotech. Geoenviron. Eng.* **134**, 1059–1072 (2008)
- Tang, X.W., Zhang, X.W.: Seismic liquefaction analysis by a modified finite element-finite difference method. *Jpn. Geotech. Soc. Spec. Publ.* **2**, 1204–1207 (2016)
- Sengara, I.W., Sulaiman, A.: Nonlinear dynamic analysis adopting effective stress approach of an embankment involving liquefaction potential. In: *E3S Web of Conferences*. p. 2018. EDP Sciences (2020)
- Huang, Y., Mao, W., Zheng, H., Li, G.: Computational fluid dynamics modeling of post-liquefaction soil flow using the volume of fluid method. *Bull. Eng. Geol. Environ.* **71**, 359–366 (2012)
- Szewc, K.: Smoothed particle hydrodynamics modeling of granular column collapse. *Granul. Matter.* **19**, 1–13 (2017)
- Nguyen, N.H.T., Bui, H.H., Nguyen, G.D.: Effects of material properties on the mobility of granular flow. *Granul. Matter.* **22**, 1–17 (2020)
- Tong, Q., Zhu, S., Yin, H.: Scale-up study of high-shear fluid-particle mixing based on coupled SPH/DEM simulation. *Granul. Matter.* **20**, 1–12 (2018)
- Salehizadeh, A.M., Shafiei, A.R.: Modeling of granular column collapses with μ (I) rheology using smoothed particle hydrodynamic method. *Granul. Matter.* **21**, 1–18 (2019)
- Hakuno, M., Tarumi, Y.: A granular assembly simulation for the seismic liquefaction of sand. *Doboku Gakkai Ronbunshu.* **1988**, 129–138 (1988)
- Wang, G., Huang, D., Wei, J.: Discrete element simulation of soil liquefaction: fabric evolution, large deformation, and multi-directional loading. In: *Geotechnical Earthquake Engineering and Soil Dynamics V: Numerical Modeling and Soil Structure Interaction*, American Society of Civil Engineers Reston, VA, pp. 123–132 (2018)
- El Shamy, U., Zeghal, M., Dobry, R., Abdoun, T., Thevanayagam, S., Elgamal, A.: DEM Simulation of Liquefaction-Induced Lateral Spreading (2010)
- Sitharam, T.G., Vinod, J.S., Ravishankar, B.V.: Post-liquefaction undrained monotonic behaviour of sands: experiments and DEM simulations. *Géotechnique.* **59**, 739–749 (2009)
- Cundall, P.A., Strack, O.D.L.: A discrete numerical model for granular assemblies. *Geotechnique.* **29**, 47–65 (1979)
- Bui, H.H., Nguyen, G.D.: Numerical predictions of post-flow behaviour of granular materials using an improved SPH model. In: *CIGOS 2019, Innovation for Sustainable Infrastructure*, Springer, pp. 895–900 (2020)
- Bui, H.H., Fukagawa, R.: An improved SPH method for saturated soils and its application to investigate the mechanisms of embankment failure: case of hydrostatic pore-water pressure. *Int. J. Numer. Anal. Methods Geomech.* **37**, 31–50 (2013)
- Chen, W., Qiu, T.: Numerical simulations for large deformation of granular materials using smoothed particle hydrodynamics method. *Int. J. Geomech.* **12**, 127–135 (2012)
- Huang, Y., Dai, Z.: Large deformation and failure simulations for geo-disasters using smoothed particle hydrodynamics method. *Eng. Geol.* **168**, 86–97 (2014)
- Islam, M.R.I., Zhang, W., Peng, C.: Large deformation analysis of geomaterials using stabilized total Lagrangian smoothed particle hydrodynamics. *Eng. Anal. Bound. Elem.* **136**, 252–265 (2022)
- Liu, G.-R., Liu, M.B.: Smoothed particle hydrodynamics: a mesh-free particle method. World scientific, Singapore (2003)
- Jiang, H., Chen, Y., Zheng, X., Jin, S., Ma, Q.: A study on stable regularized moving least-squares interpolation and coupled with SPH method. *Math. Probl. Eng.* **2020**, 1 (2020)
- Huang, C., Lei, J.M., Liu, M.B., Peng, X.Y.: A kernel gradient free (KGF) SPH method. *Int. J. Numer. Methods Fluids.* **78**, 691–707 (2015)
- Johnson, G.R., Beissel, S.R.: Normalized smoothing functions for SPH impact computations. *Int. J. Numer. Methods Eng.* **39**, 2725–2741 (1996)
- Monaghan, J.J.: Simulating free surface flows with SPH. *J. Comput. Phys.* **110**, 399–406 (1994)
- Monaghan, J.J.: Smoothed particle hydrodynamics. *Rep. Prog. Phys.* **68**, 1703 (2005)
- Ionescu, I.R., Mangeney, A., Bouchut, F., Roche, O.: Viscoplastic modeling of granular column collapse with pressure-dependent rheology. *J. NonNewton. Fluid Mech.* **219**, 1–18 (2015)
- Minatti, L., Paris, E.: A SPH model for the simulation of free surface granular flows in a dense regime. *Appl. Math. Model.* **39**, 363–382 (2015)
- Moriguchi, S., Borja, R.I., Yashima, A., Sawada, K.: Estimating the impact force generated by granular flow on a rigid obstruction. *Acta Geotech.* **4**, 57–71 (2009)
- Bui, H.H., Fukagawa, R., Sako, K., Ohno, S.: Lagrangian mesh-free particles method (SPH) for large deformation and failure flows of geomaterial using elastic–plastic soil constitutive model. *Int. J. Numer. Anal. Methods Geomech.* **32**, 1537–1570 (2008)
- Bui, H.H., Sako, K., Fukagawa, R.: Numerical simulation of soil–water interaction using smoothed particle hydrodynamics (SPH) method. *J. Terramech.* **44**, 339–346 (2007)
- Libersky, L.D., Petschek, A.G., Carney, T.C., Hipp, J.R., Allahdadi, F.A.: High strain Lagrangian hydrodynamics: a three-dimensional SPH code for dynamic material response. *J. Comput. Phys.* **109**, 67–75 (1993)
- Monaghan, J.J.: SPH without a tensile instability. *J. Comput. Phys.* **159**, 290–311 (2000)
- Gray, J.P., Monaghan, J.J., Swift, R.P.: SPH elastic dynamics. *Comput. Methods Appl. Mech. Eng.* **190**, 6641–6662 (2001)

36. Monaghan, J.J., Pongracic, H.: Artificial viscosity for particle methods. *Appl. Numer. Math.* **1**, 187–194 (1985)
37. Di, Y., Sato, T.: Liquefaction analysis of saturated soils taking into account variation in porosity and permeability with large deformation. *Comput. Geotech.* **30**, 623–635 (2003)
38. Zienkiewicz, O.C., Shiomi, T.: Dynamic behaviour of saturated porous media; the generalized Biot formulation and its numerical solution. *Int. J. Numer. Anal. Methods Geomech.* **8**, 71–96 (1984)
39. Singh, A.P., Borke, R.D.: Smoothed particle hydrodynamics. *Dep. Aerosp. Eng. Indian Inst. Technol* (2010)
40. Issakhov, A., Zhandaulet, Y., Nogaeva, A.: Numerical simulation of dam break flow for various forms of the obstacle by VOF method. *Int. J. Multiph. Flow.* **109**, 191–206 (2018)
41. Amicarelli, A., Manenti, S., Paggi, M.: SPH modelling of dam-break floods, with damage assessment to electrical substations. *Int. J. Comput. Fluid Dyn.* **35**, 1–19 (2020)
42. Li, D., Zheng, D., Wu, H., Shen, Y., Nian, T.: Numerical simulation on the longitudinal breach process of landslide dams using an improved coupled DEM-CFD method. *Front. Earth Sci.* **9**, 315 (2021)
43. Lobovský, L., Botia-Vera, E., Castellana, F., Mas-Soler, J., Souto-Iglesias, A.: Experimental investigation of dynamic pressure loads during dam break. *J. Fluids Struct.* **48**, 407–434 (2014)
44. Jamshidi Chenari, R., Yousefi Barandagh, A., Esfandiari, M.B.: Investigation into the effect of carpet fiber inclusion on the pore water pressure generation potential of sand in a quick tank. *Sharif J. Civ. Eng.* **31**, 133–140 (2015)
45. Ahmadi, H., Eslami, A., Arabani, M.: Characterization of sedimentary Anzali Sand for static and seismic studies purposes. *Int. J. Geogr. Geol.* **4**, 155–169 (2015)
46. Tsuchida, H.: Prediction and countermeasure against the liquefaction in sand deposits. In: *Abstract of the Seminar in the Port and Harbor Research Institute*, pp. 31–333 (1970)
47. Sandeep, C.S., Senetakis, K.: Effect of Young's modulus and surface roughness on the inter-particle friction of granular materials. *Materials* **11**(2), 217 (2018)
48. Sandeep, C.S., He, H.: Senetakis K (2022) Experimental and analytical studies on the influence of weathering degree and ground-environment analog conditions on the tribological behavior of granite. *Eng. Geol.* **304**, 106644 (2022)
49. Kokusho, T., Takahashi, T.: Earthquake-induced submarine landslides in view of void redistribution. In: *Geotechnical Engineering for Disaster Mitigation and Rehabilitation*, Springer, pp. 177–188 (2008)
50. Alaie, R., Jamshidi Chenari, A.: Design and performance of a single axis shake table and a laminar soil container. *Civ. Eng. J.* **4**, 1326–1337 (2018)
51. Fathi, H., Jamshidi Chenari, A.: Shaking table study on PET strips-sand mixtures using laminar box modelling. *Geotech. Geol. Eng.* **38**(1), 683–694 (2020)
52. Maghsoudi, M.S., Jamshidi Chenari, R., Farrokhi, F.: A multilateral analysis of slope failure due to liquefaction-induced lateral deformation using shaking table tests. *SN Appl. Sci.* **2**(8), 1–11 (2020). <https://doi.org/10.1007/s42452-020-03234-8>
53. Kokusho, T.: Water film in liquefied sand and its effect on lateral spread. *J. Geotech. Geoenviron. Eng.* **125**, 817–826 (1999)
54. Polito, C.P., Moldenhauer, H.H.M.: Pore pressure generation and dissipated energy ratio in cohesionless soils. In: *Geotechnical Earthquake Engineering and Soil Dynamics V: Slope Stability and Landslides, Laboratory Testing, and In Situ Testing*, American Society of Civil Engineers Reston, VA, pp. 336–344 (2018)
55. Davis, R.O., Berrill, J.B.: Pore pressure and dissipated energy in earthquakes—field verification. *J. Geotech. Geoenviron. Eng.* **127**, 269–274 (2001)
56. Figueroa, J.L., Saada, A.S., Liang, L., Dahisaria, N.M.: Evaluation of soil liquefaction by energy principles. *J. Geotech. Eng.* **120**, 1554–1569 (1994)
57. Towhata, I., Ishihara, K.: Shear work and pore water pressure in undrained shear. *Soils Found.* **25**, 73–84 (1985)
58. Ishac, M.F., Heidebrecht, A.C.: Energy dissipation and seismic liquefaction in sands. *Earthq. Eng. Struct. Dyn.* **10**, 59–68 (1982)
59. Liu, M., Li, G., Zhang, J., Liu, J., Yang, Z.: Relationship between pore water pressure and dissipated energy of fiber-reinforced sand. In: *IOP Conference Series: Earth and Environmental Science*, IOP Publishing, p. 12105 (2021)
60. Zeghal, M., Elgamal, A.-W.: Analysis of site liquefaction using earthquake records. *J. Geotech. Eng.* **120**, 996–1017 (1994)
61. Jamshidi, R., Towhata, I., Ghiassian, H., Tabarsa, A.R.: Experimental evaluation of dynamic deformation characteristics of sheet pile retaining walls with fiber reinforced backfill. *Soil Dyn. Earthq. Eng.* **30**, 438–446 (2010)
62. Taboada-Urtuzuastegui, V.M., Dobry, R.: Centrifuge modeling of earthquake-induced lateral spreading in sand. *J. Geotech. Geoenviron. Eng.* **124**, 1195–1206 (1998)

Publisher's Note Springer Nature remains neutral with regard to jurisdictional claims in published maps and institutional affiliations.

Springer Nature or its licensor holds exclusive rights to this article under a publishing agreement with the author(s) or other rightsholder(s); author self-archiving of the accepted manuscript version of this article is solely governed by the terms of such publishing agreement and applicable law.